JCI insight

RESEARCH ARTICLE

# Junctophilin-2 expression rescues atrial dysfunction through polyadic junctional membrane complex biogenesis

**Sören Brandenburg,[1] Jan Pawlowitz,[1] Benjamin Eikenbusch,[1] Jonas Peper,[1] Tobias Kohl,[1] Gyuzel Y. Mitronova,[2] Samuel Sossalla,[1] Gerd Hasenfuss,[1,3] Xander H.T. Wehrens,[4] Peter Kohl,[5] Eva A. Rog-Zielinska,[5] and Stephan E. Lehnart[1,3,6]**

[1]Heart Research Center Göttingen, Department of Cardiology & Pneumology, University Medical Center Göttingen, Göttingen, Germany. [2]Department of NanoBiophotonics, Max Planck Institute for Biophysical Chemistry, Göttingen, Germany. [3]DZHK (German Centre for Cardiovascular Research), partner site Göttingen, Germany. [4]Cardiovascular Research Institute – Department of Molecular Physiology and Biophysics, Baylor College of Medicine, Houston, Texas, USA. [5]University Heart Center, Faculty of Medicine, University of Freiburg, Freiburg im Breisgau, Germany. [6]BioMET, Center for Biomedical Engineering and Technology, University of Maryland School of Medicine, Baltimore, Maryland, USA.

**Atrial dysfunction is highly prevalent and associated with increased severity of heart failure. While rapid excitation-contraction coupling depends on axial junctions in atrial myocytes, the molecular basis of atrial loss of function remains unclear. We identified approximately 5-fold lower junctophilin-2 levels in atrial compared with ventricular tissue in mouse and human hearts. In atrial myocytes, this resulted in subcellular expression of large junctophilin-2 clusters at axial junctions, together with highly phosphorylated ryanodine receptor (RyR2) channels. To investigate the contribution of junctophilin-2 to atrial pathology in adult hearts, we developed a cardiomyocyte-selective junctophilin-2–knockdown model with 0 mortality. Junctophilin-2 knockdown in mice disrupted atrial RyR2 clustering and contractility without hypertrophy or interstitial fibrosis. In contrast, aortic pressure overload resulted in left atrial hypertrophy with decreased junctophilin-2 and RyR2 expression, disrupted axial junctions, and atrial fibrosis. Whereas pressure overload accrued atrial dysfunction and heart failure with 40% mortality, additional junctophilin-2 knockdown greatly exacerbated atrial dysfunction with 100% mortality. Strikingly, transgenic junctophilin-2 overexpression restored atrial contractility and survival through de novo biogenesis of polyadic junctional membrane complexes maintained after pressure overload. Our data show a central role of junctophilin-2 cluster disruption in atrial hypertrophy and identify transgenic augmentation of junctophilin-2 as a disease-mitigating rationale to improve atrial dysfunction and prevent heart failure deterioration.**

## Introduction

Atrial fibrillation and chronic heart failure frequently coexist in patients. Importantly, once combined, atrial fibrillation with heart failure results in significantly increased morbidity, mortality, and more frequent drug treatment failure (1–4). The prevalence of both atrial fibrillation and heart failure is increasing (5), with atrial fibrillation alone predicted to rise 3-fold in octogenarians by 2050 (6). In line with this, electrical and contractile dysfunction of the atria is most prevalent in elderly people, increasing the risk each for atrial fibrillation, heart failure, and stroke (6). Recently, atrial myocyte (AM) dysfunction was recognized as a causative proximal factor of adverse cardiac remodeling in the absence of or preceding atrial fibrillation (7). This concept is further supported by recently identified rare mutations in sarcomeric genes, *MYL4* and *TTN,* associated for the first time with atrial cardiomyopathies in patients (8, 9). Although atrial dysfunction is increasingly recognized as a common cause of the growing disease burden (7), the underlying mechanisms are not well understood (10, 11).

Important for active ventricular filling and hemodynamic stress adaptation, the atrial "kick," a specialized form of cardiovascular function occurs through earlier atrial activation and faster atrial than ventricular contraction (12, 13). Both in AMs and ventricular myocytes (VMs), contractile activation is highly regulated: opening of voltage-gated L-type $Ca^{2+}$ channels in the sarcolemma leads to $Ca^{2+}$ influx,

**Conflict of interest:** SEL is an inventor on a patent (US 20070089572A1) submitted by Columbia University "Novel agents for preventing and treating disorders involving modulation of RYR receptors."



**Submitted:** January 2, 2019
**Accepted:** May 16, 2019
**Published:** June 20, 2019.

**Reference information:** *JCI Insight*. 2019;4(12):e127116. https://doi.org/10.1172/jci.insight.127116.

subsequently activating a much larger $Ca^{2+}$ release from the sarcoplasmic reticulum (SR) via ryanodine receptor 2 (RyR2) channels — a process referred to as $Ca^{2+}$-induced $Ca^{2+}$ release (CICR; ref. 10). For efficient CICR and excitation-contraction coupling, junctophilin-2, a tail-anchored protein located in the SR membrane, is necessary to physically tether the sarcolemmal membrane to within a proximity of 15 nm through its N-terminal "membrane occupation and recognition nexus" (MORN) domains (14, 15). In addition to its structural role, junctophilin-2 stabilizes the closed state of RyR2 channels, while increased SR $Ca^{2+}$ leak, ventricular hypertrophy, and heart failure were associated with decreased junctophilin-2 expression in patients and mice (15–17). Additionally, atrial fibrillation and hypertrophic cardiomyopathy were linked to rare junctophilin-2 mutations in patients (18, 19). However, the atrial cell biology of junctophilin-2 and its significance for AM-specific pathomechanisms in the context of common, acquired forms of atrial cardiomyopathy are basically unknown.

Because junctional RyR2 channel clusters were previously visualized strictly at the outer surface but not inside AMs (20), we wondered whether atrial junctophilin-2 expression follows the same pattern. Recently, however, a novel atria-specific excitation-contraction mechanism was discovered based on extensive axial tubule (AT) junctions that rapidly activate $Ca^{2+}$ release deep inside AMs (12). Consequently, as AT membrane structures are conserved across species from mouse to human atria (21), we hypothesized that junctophilin-2 is differentially distributed between AT junctional versus nonjunctional RyR2 clusters in AMs. Remarkably, in mouse and human hearts, we found approximately 5 times lower atrial compared with ventricular junctophilin-2 protein levels. Aortic pressure overload in mice further reduced atrial junctophilin-2 expression and severely disrupted junctional membrane complexes (JMCs). Atrial junctophilin-2 downregulation was confirmed as a pathomechanism of disrupted JMCs by shRNA-mediated knockdown, leading to atrial dysfunction with severely aggravated heart failure in vivo. Importantly, junctophilin-2 overexpression (JP2-OE) reversed the atrial dysfunction, fibrosis, and excess mortality following left heart pressure overload. In AMs, we discovered that JP2-OE induced the biogenesis of large polyadic JMCs, a junctional superstructure that remained functionally preserved after pressure overload. Thus, whereas decreased junctophilin-2 expression impaired atrial excitation-contraction coupling, transgenic junctophilin-2 expression rescued RyR2 clustering, $Ca^{2+}$ signaling, and atrial contractility, providing a rationale for biomimetic junctophilin-2 augmenting interventions to treat atrial dysfunction and slow heart failure deterioration.

## Results

*Atria-specific subcellular junctophilin-2 organization*. While knockdown of 60% of ventricular junctophilin-2 causes acute heart failure with 40% mortality within 1 week (15), atrial junctophilin-2 protein expression, its relation to ventricular levels, and the significance for subcellular $Ca^{2+}$ release domains in AMs is currently unknown. To address this question, we compared junctophilin-2 and RyR2 protein levels in paired atrial and ventricular mouse cardiac tissue samples. Unexpectedly, atrial compared with ventricular junctophilin-2 expression was approximately 5 times lower, while RyR2 expression was similar (Figure 1A and Supplemental Figure 1; supplemental material available online with this article; https://doi.org/10.1172/JCI127116DS1). This resulted in a significantly reduced atrial junctophilin-2/RyR2 ratio (Figure 1A). As junctophilin-2 knockdown disrupts RyR2 channel closure and increases SR $Ca^{2+}$ leak in VMs (15), we asked how AMs maintain excitation-contraction coupling subcellularly in spite of a vast stoichiometric junctophilin-2/RyR2 expression difference.

Confocal immunofluorescence imaging showed that junctophilin-2 is differentially distributed in AMs: larger junctophilin-2 cluster signals are mainly associated with axially oriented tubules (ATs) identified by caveolin-3 costaining, in contrast with smaller transversal junctophilin-2 signals (Figure 1B). Total cell 3D-projection analysis confirmed robust colocalization of large junctophilin-2 clusters with junctional RyR2 clusters deep inside and along the main axis of AMs, transecting striations of transversal RyR2 clusters (Figure 1C). Reminiscent of the junctophilin-2 cluster distribution, antibody-labeling specific for PKA-phosphorylated RyR2-Ser2808 (12) revealed a similar 3D pattern for highly phosphorylated RyR2 clusters (Figure 1D). Finally, triple staining confirmed that large junctophilin-2 clusters overlap with highly phosphorylated RyR2 clusters along axially oriented tracks in AMs (Supplemental Figure 2A) but not in VMs (Supplemental Figure 2B).

To resolve the 3D nature of the AT-associated RyR2 clusters, we investigated semi-thick sections (280 nm) of high-pressure frozen AMs by electron tomography (ET) (12, 22). ET showed voluminous AT membrane structures located next to myofilaments (Figure 1E). As highlighted by color rendering, the AT membrane structures (green) were occupied by axial SR junctions (red), henceforth defined as AT-SR

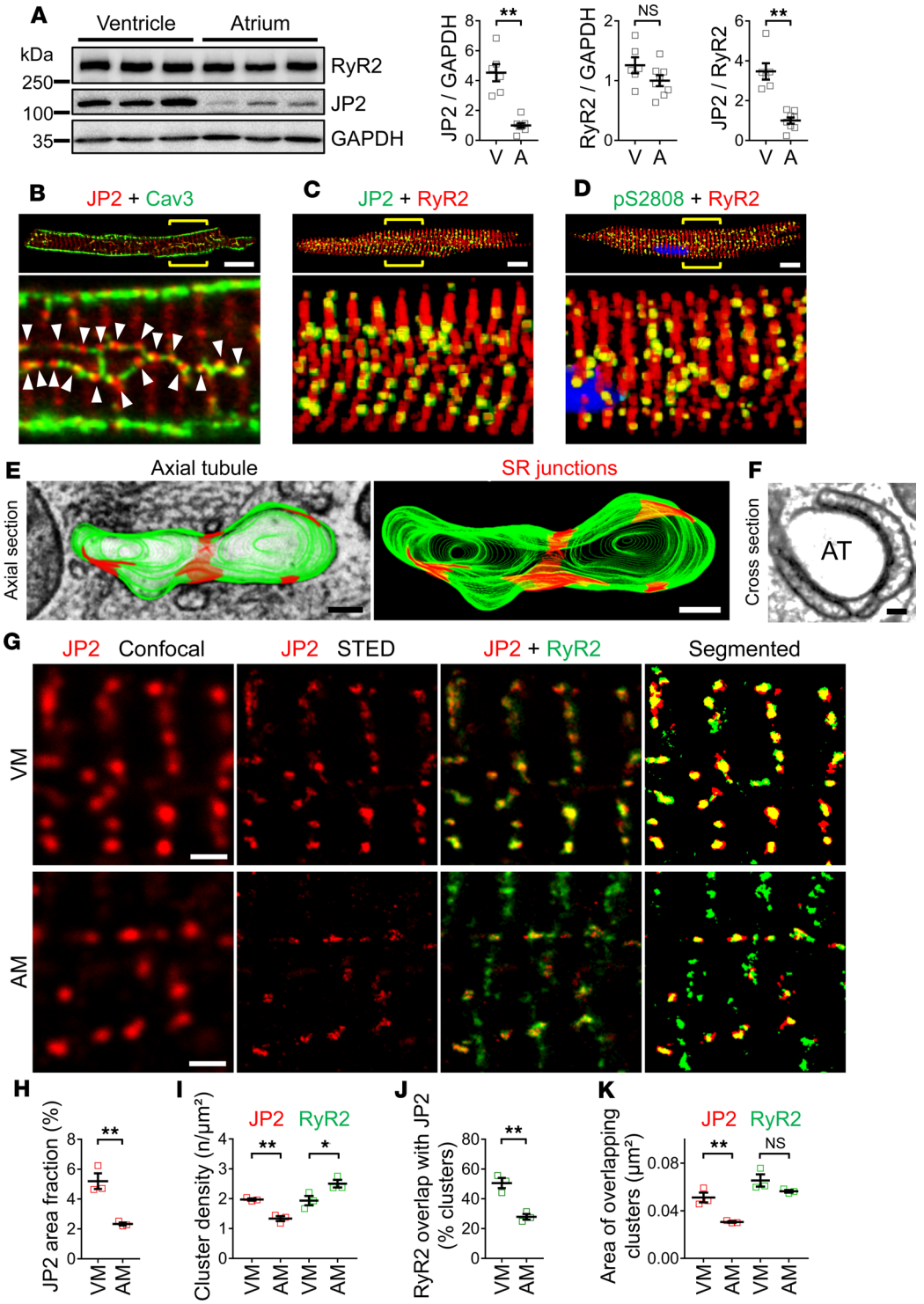


**Figure 1. Junctophilin-2 clustering at axial tubules in atrial myocytes.** (**A**) Junctophilin-2 (JP2) and ryanodine receptor (RyR2) immunoblots of ventricular versus atrial tissue. Unexpectedly, atrial JP2 is approximately 5-fold below ventricular levels. Dot plots are representative of 3 independent experiments. (**B**) Confocal imaging showing heterogeneous JP2 distribution in AMs. Larger JP2 clusters (arrowheads) occur at axial tubules (ATs) labeled with caveolin-3 (Cav3). Scale bar: 10 µm. (**C**) Confocal 3D projection shows JP2 clusters deep inside AMs, intersecting RyR2 clusters in transversal striations. Large JP2 clusters are distributed similar to (**D**) highly PKA phosphorylated RyR2 clusters. Nucleus, blue (DAPI). Yellow brackets indicate magnified regions. Scale bars: 10 µm. (**E**) ET images of longitudinally sectioned and (**F**) cross-sectioned AT structures were used for 3D reconstruction of AT-SR junctions. Scale bar: 100 nm. Red, AT-SR junctions ≤15 nm in gap width and containing RyR2-like densities; green, membrane area without apparent AT-SR junctions. (**G**) STED superresolution imaging of JP2 and RyR2 clusters in ventricular (VM) and atrial myocytes (AM). STED images were segmented (right) for detailed cluster analysis. Scale bar: 1 µm. Both the (**H**) JP2 area fraction and (**I**) cluster density were smaller in AMs compared with VMs. In contrast, RyR2 cluster density was significantly higher in AMs. (**J**) Only 28% of atrial RyR2 clusters overlap with JP2 cluster signals, and (**K**) overlapping JP2 clusters in AMs were significantly smaller compared with VMs. $n$ = 3 individual hearts each for 17 VM and 15 AM cells. *$P$ < 0.05; **$P$ < 0.01, Student's $t$ test.

junction, within less than 15 nm and containing clusters of electron-dense nanostructures (Figure 1E). Consistently, AT cross sections showed junctional gaps densely filled with RyR2-compatible structures covering substantial areas of the cytosolic AT circumference (Figure 1F).

To further investigate the relationship between the junctophilin-2 and RyR2 clusters, we used dual-color STimulated Emission Depletion (STED) superresolution microscopy. In VMs, junctophilin-2 clusters were highly colocalized with RyR2 clusters in transversal striations (Figure 1G) as expected (23). In contrast, larger junctophilin-2 clusters were less abundant in AMs (Figure 1G). Consistent with an approximately 5-fold lower junctophilin-2/RyR2 ratio, larger RyR2 clusters only occasionally colocalized with larger junctophilin-2 clusters in AMs, as highlighted by image segmentation (Figure 1G, right). Image analysis confirmed a significantly decreased junctophilin-2 area fraction (Figure 1H) and cluster density in AMs compared with VMs, despite a higher atrial RyR2 cluster density (Figure 1I). Quantitatively, in AMs only 28% of RyR2 clusters overlapped with junctophilin-2 signals (Figure 1J). Finally, the area of junctophilin-2 clusters overlapping with RyR2 clusters was significantly smaller in AMs compared with VMs (Figure 1K). Hence, although junctophilin-2 protein levels are significantly lower in AMs, larger junctophilin-2 clusters exist and overlap with approximately every fourth RyR2 cluster, yet mainly at AT-SR junctions.

*Junctophilin-2 cluster organization in human atria*. In paired left heart tissue samples, atrial compared with ventricular junctophilin-2 expression was 76% lower in human myocardium, resulting in a significantly decreased junctophilin-2/RyR2 ratio (Figure 2A and Supplemental Figure 1). Next, we used STED microscopy of human tissue sections to investigate junctophilin-2 clustering in situ in AMs. Interestingly, atrial tissue from patients with chronic atrial fibrillation and aortic stenosis undergoing surgical valve replacement showed randomly distributed AT fragments and dispersed small junctophilin-2 clusters (Figure 2B) or subcellular areas completely devoid of either immunofluorescence signal (Figure 2B). In contrast, AMs from patients in sinus rhythm showed robust junctophilin-2 clustering associated with abundant AT structures, whereas VMs were dominated by abundant junctophilin-2 clusters along transverse tubules (TTs; Figure 2C). These observations suggest that chronic hemodynamic stress from aortic valve stenosis may lead to disruption of left atrial junctophilin-2 clustering and AT-SR junctions in the left atria of patients.

*Aortic constriction pressure overload disrupts AT-SR junctions*. To investigate junctophilin-2 clustering during chronically increased hemodynamic stress, we used a mouse model of transaortic constriction (TAC) to induce left atrial hypertrophy as reported previously (12). Four weeks after TAC, a profound decrease in the levels of caveolin-3, junctophilin-2, and RyR2 was observed in left atrial tissue (Figure 3A and Supplemental Figure 1). Interestingly, after TAC 3 of 27 mice (11%) spontaneously alternated between sinus and irregular rhythms (Supplemental Figure 3), indicating a paroxysmal form of arrhythmia susceptibility that requires future in-depth investigation.

Second, in the context of numerical AT proliferation after TAC, as reported previously (12), dual-color STED imaging identified apparent changes in AT-associated junctophilin-2 clustering (Figure 3B). Yet, STED superresolution microscopy also showed a pronounced dispersion of junctional junctophilin-2 and RyR2 clusters at AT structures, where the latter remained highly PKA phosphorylated (Figure 3, C and D).

Consistent with decreased junctophilin-2 and RyR2 expression, image analysis revealed a significantly decreased RyR2 area fraction (Figure 3E) and cluster density after TAC (Figure 3F). Interestingly, whereas the overlap of junctophilin-2 clusters with RyR2 clusters was significantly decreased, the inverse overlap — i.e., the fraction of RyR2 clusters associated with junctophilin-2 clusters — was increased (Figure 3G), indicating a multifactorial mechanism. Finally, the signal area of junctophilin-2 clusters overlapping with RyR2 clusters, and vice versa, was not changed (Figure 3H). Together with greatly decreased junctophilin-2 and RyR2 expression (Figure 3A), these data illustrate profound molecular clustering changes suggesting a loss of junctionally competent JMCs after TAC.

Furthermore, ET and 3D reconstruction of AT cross sections revealed local membrane-proliferative cytoplasmic protrusions after TAC (Figure 3I, green). Importantly, whereas RyR2-filled AT-SR junctions were apparent in left AMs from sham hearts, after TAC hearts showed diminished junctional structures (Figure 3I, red; gap size ≤15 nm). Quantitatively, a significantly decreased AT-SR junction length and junction surface were evident (Figure 3J). In summary, we hypothesize that depressed left atrial contractility after pressure overload is at least in part explained by disruption of AT-SR junctions and diminished junctophilin-2 and RyR2 expression, leading to increased junctional cluster dispersion at the cost of decreased contractile function.

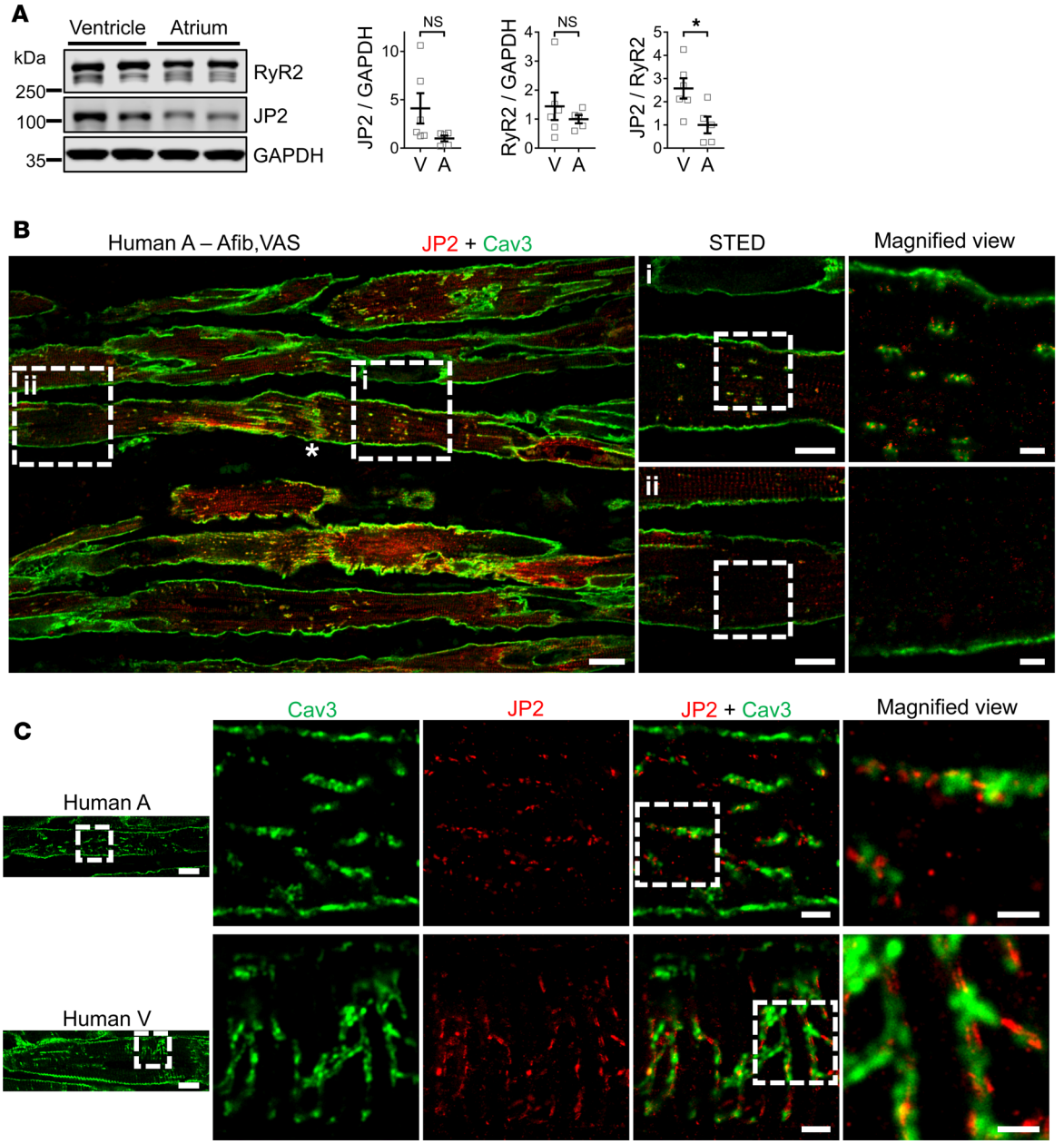


**Figure 2. Junctophilin-2 clustering in human atrial and ventricular tissue sections.** (**A**) Immunoblotting of human left heart tissue lysates reveals significantly reduced atrial expression of junctophilin-2 (JP2) relative to RyR2. Representative data from paired left atrial and left ventricular tissue samples; $n = 6$ hearts. $^*P < 0.05$, Student's $t$ test. (**B**) STED superresolution imaging of human left atrial myocytes in situ. Histology section from a patient with chronic atrial fibrillation (Afib) and valvular aortic stenosis (VAS) undergoing aortic valve replacement. Note randomly distributed small AT fragments and dispersed JP2 clustering. The asterisk indicates an intercalated disc between adjacent AMs magnified. Scale bars: 20 μm (left); 10 μm (middle); 1 μm (right). (**C**) In situ visualization of right atrial (A) and left ventricular (V) myocytes in histology sections from hearts in sinus rhythm ($n = 2$). STED coimmunofluorescence imaging showing caveolin-3–labeled membrane structures and JP2 clusters. Note different orientations between abundant AT structures in magnified AM versus TT structures in magnified VM and their relationship with JP2 clusters. Dashed boxes indicate magnified regions (right). Scale bars: 10 μm (left); 2 μm (middle);1 μm (right). Please see Supplemental Methods and Supplemental Table 3 for detailed clinical patient information.

*Junctophilin-2 knockdown causes atrial dysfunction.* To selectively decrease junctophilin-2 expression in adult hearts, we adapted a double-transgenic strategy using the cardiac-specific α-myosin heavy chain (αMHC) promotor and tamoxifen-inducible junctophilin-2 knockdown targeted by shRNA (shJP2; ref. 15). By decreasing the concentration and/or duration of intraperitoneal tamoxifen dosing, we titrated the MerCreMer-based (MCM-based) model toward a significant reduction in atrial junctophilin-2 expression, while avoiding any excess mortality as observed for higher tamoxifen doses

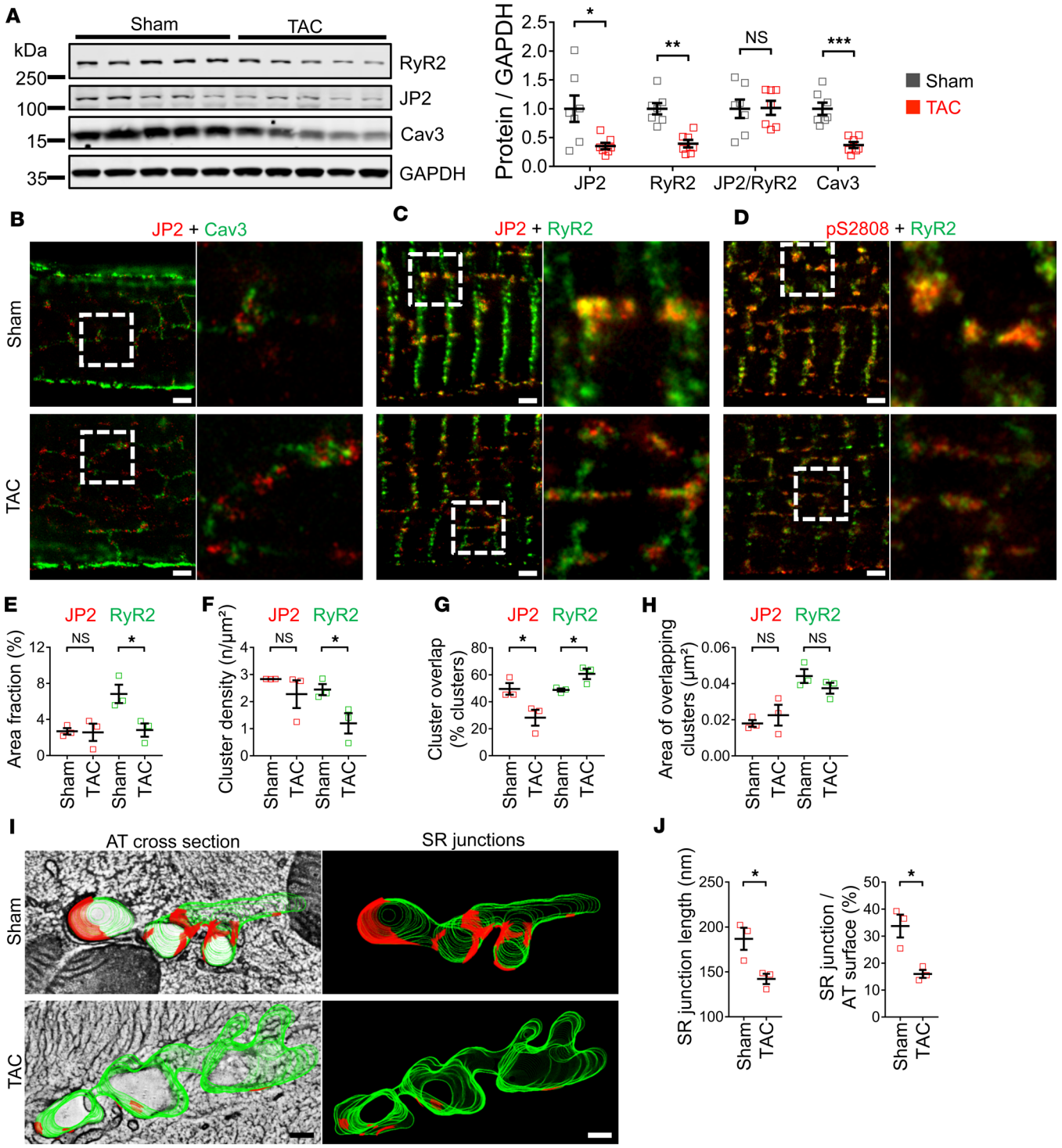


**Figure 3. Left atrial junctophilin-2 cluster dispersion, RyR2 cluster decrease, and AT proliferation in aortic pressure overload.** (**A**) Immunoblots show reduced left atrial expression of junctophilin-2 (JP2), RyR2, and caveolin-3 4 weeks after TAC. Data represent 3 independent experiments each for sham and TAC. (**B**–**D**) Dual-color STED immunofluorescence imaging of isolated left AMs 4 weeks after TAC labeled for JP2, caveolin-3, RyR2, and phospho-epitope specific RyR2-pSer2808. (**B**) Caveolin-3–positive axial tubules increase in number after TAC, and junctional JP2 clusters appear dispersed at axial tubules. (**C**) JP2 colocalization with RyR2 is decreased after TAC. (**D**) Highly phosphorylated RyR2-pS2808 clusters decrease in size after TAC. Dashed boxes indicate magnified views on the right. Scale bar: 1 µm. (**E**–**H**) Analysis of segmented STED images. RyR2 area fraction (**E**) and RyR2 cluster density (**F**) were significantly decreased after TAC. (**G**) TAC induced a significant increase in percentage overlap of RyR2 with JP2 clusters, while percentage overlap of JP2 with RyR2 clusters was decreased. (**H**) The areas of overlapping JP2 and RyR2 clusters were statistically unchanged after TAC. $n$ = 3 individual hearts each; 17 sham and 13 TAC AM cells. (**I**) ET 3D reconstruction of cross-sectioned AT structures (green) and AT-SR junctions (red, ≤15 nm in gap width filled with RyR2 densities). Scale bar: 200 nm. (**J**) AT-SR junction length and the proportion of AT-SR junction area relative to the AT surface are significantly reduced after TAC. $n$ = 3 individual hearts each. $^{*}P < 0.05$; $^{**}P < 0.01$; $^{***}P < 0.001$, Student's $t$ test.

previously (Supplemental Figure 4 and ref. 15). Here, a single tamoxifen injection (40 mg/kg) significantly decreased atrial junctophilin-2 expression from 100% to 43% within 2 weeks in MCM-shJP2 mice compared with MCM control mice, respectively (Figure 4A and Supplemental Figure 1); hence this intervention was used throughout the data reported below. While RyR2 protein expression was unchanged, the junctophilin-2/RyR2 ratio was significantly decreased (Figure 4A). Importantly, in AMs, junctophilin-2 knockdown caused a decrease in RyR2-Ser2808 phosphorylation, while caveolin-3 and the SR $Ca^{2+}$-ATPase (SERCA2a) were significantly increased (Figure 4A).

Parasternal long-axis echocardiography with simultaneous ECG recording, as described previously (12), was used to characterize atrial contractile function after junctophilin-2 knockdown (Figure 4B). While the left atrial diameter was unchanged, fractional shortening was significantly decreased (Figure 4C). Whereas the left ventricular diameter remained unchanged, left ventricular ejection fraction was decreased in MCM-shJP2 mice (Figure 4D). Notably, left atrial histological sections stained with hematoxylin and eosin or Sirius red/fast green excluded substantial interstitial fibrosis after junctophilin-2 knockdown (Supplemental Figure 5). Thus, despite significant SERCA2a upregulation, atrial junctophilin-2 knockdown resulted in reduced contractile function.

*Atrial junctophilin-2 knockdown induces AT proliferation and disrupts JMCs*. Two weeks after junctophilin-2 knockdown induction, isolated AMs from MCM and MCM-shJP2 mice were used for live-cell imaging (Figure 5, A and B). AM length, width, and length-to-width ratios were not changed after junctophilin-2 knockdown (Supplemental Figure 6), consistent with normal left atrial size (Figure 4C) and tissue structure (Supplemental Figure 5). However, the transverse-axial-tubule (TAT) network appeared fundamentally reorganized (Figure 5B). The number of ATs tended to be increased at the cost of TTs, as shown by histogram subtraction (MCM-shJP2 minus MCM data; Figure 5, C and D). This resulted in an increased TAT network density (Figure 5D), consistent with AT-dependent membrane proliferation and increased caveolin-3 expression (Figure 4A).

Dual-color STED microscopy showed more disperse and smaller junctophilin-2 clusters at caveolin-3–labeled AT-SR junctions, together with smaller RyR2 clusters following knockdown (Figure 5, E and F). Interestingly, despite the decreased protein level, the area fraction of junctophilin-2 signals was not significantly changed, which might be explained by increased junctophilin-2 cluster dispersion (Figure 5G). In contrast, the RyR2 cluster area fraction was decreased by junctophilin-2 knockdown, whereas RyR2 overlap with junctophilin-2 clusters was unchanged (Figure 5, G and H). Finally, the area of RyR2 clusters overlapping with junctophilin-2 clusters was markedly decreased, while the inverse overlap — i.e., the fraction of junctophilin-2 signal associated with RyR2 signal — was unchanged (Figure 5I). Hence, in addition to AT membrane proliferation, junctophilin-2 knockdown leads to decreased junctional RyR2 clustering, directly explaining the decreased local IF cluster signal and global decrease in RyR2-Ser2808 channel phosphorylation (Figure 4A).

*Cardiac junctophilin-2 knockdown increases atrial $Ca^{2+}$ leak*. To explore the functional consequence of junctional RyR2 cluster disruption, we measured AT-associated $Ca^{2+}$ release events in AMs following junctophilin-2 knockdown. Transverse line scanning of the $Ca^{2+}$ signal (fluo-4-AM 10 μM) was combined with membrane labeling (Cholesterol-PEG-KK114 1 μM), as described previously (21). $Ca^{2+}$ transients, $Ca^{2+}$ sparks and their relation with different membrane structures were visualized (Figure 6A). AMs from MCM or MCMshJP2 hearts showed similar $Ca^{2+}$ transients (Figure 6B) and there were no significant differences in the amplitude, time to peak, duration, or decay (Figure 6C). Interestingly, whereas atrial junctophilin-2 knockdown via AAV9 gene transfer resulted in a decreased $Ca^{2+}$ transient amplitude and SR load 4 weeks after treatment (24), increased compensatory SERCA2a expression in our shJP2-knockdown model (Figure 4A) may preserve the $Ca^{2+}$ transient amplitude.

However, the number of $Ca^{2+}$ sparks fired repeatedly from AT sites was apparently increased after junctophilin-2 knockdown (Figure 6A), contributing to a globally increased $Ca^{2+}$ spark frequency (Figure 6D). When we normalized the frequency of AT-associated $Ca^{2+}$ sparks to the number of ATs, the difference between MCM and MCM-shJP2 was diminished, consistent with a functional role of numerical AT proliferation (Figure 6E). In addition, we compared subsurface and AT membrane locations, finding higher $Ca^{2+}$ spark frequencies at AT membranes after junctophilin-2 knockdown; however, the $Ca^{2+}$ spark frequency was approximately 2-fold higher at AT compared with subsurface sites (Figure 6F). Thus, diastolic SR $Ca^{2+}$ leak through $Ca^{2+}$ sparks was increased mainly at AT sites after atrial junctophilin-2 knockdown and might be explained by AT proliferation together with junctional and functional RyR2 cluster changes.

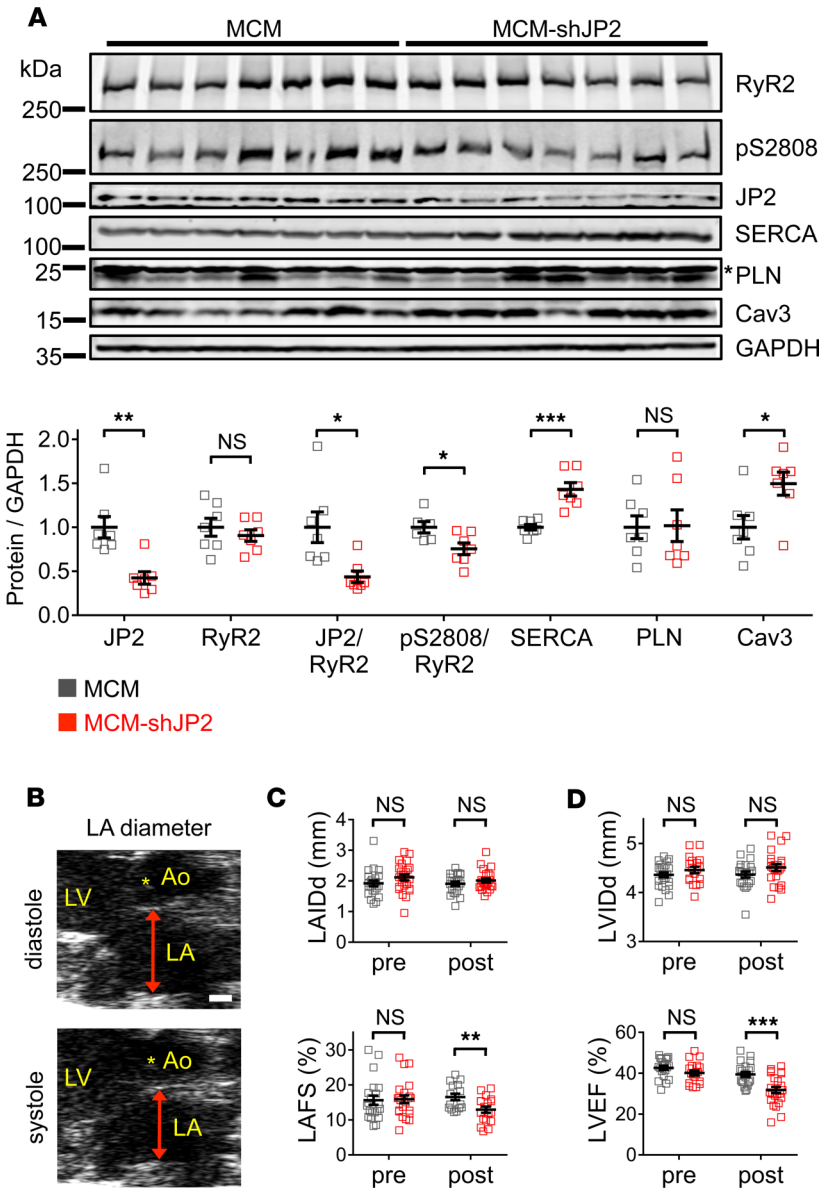


**Figure 4. shRNA-mediated junctophilin-2 knockdown induces atrial dysfunction.** (**A**) Immunoblots of atrial tissue lysates showing control (MCM) versus shRNA-mediated junctophilin-2 (JP2) knockdown (MCM-shJP2) in adult mice 2 weeks after tamoxifen treatment (40 mg/kg). JP2 expression and the JP2/RyR2 ratio after TAC were significantly reduced, concomitant with decreased RyR2-pS2808 phosphorylation. In contrast, expression of SERCA2a and caveolin-3 were significantly increased. Data represent at least 3 independent experiments. (**B**) Left atrial (LA) echocardiography long-axis view. LV, left ventricle; Ao, aorta; asterisk, aortic valve. Scale bar: 0.5 mm. (**C**) Dot plots summarizing individual echocardiographic left atrial measurements before (pre) and 2 weeks after (post) tamoxifen application. While fractional shortening was significantly decreased, LA dimensions were not changed. (**D**) LV ejection fraction was significantly decreased in structurally normal hearts. IDd, inner diameter in diastole; FS, fractional shortening; EF, ejection fraction. $n$ = 16 MCM and 18 MCM-shJP2 mice. *$P$ < 0.05; **$P$ < 0.01; ***$P$ < 0.001, Student's $t$ test.

*JP2-OE enhances atrial function*. Overexpression of junctophilin-2 was previously shown to attenuate TT reorganization and heart failure progression in ventricular disease models associated with decreased junctophilin-2 expression (15, 25). Due to approximately 5-fold lower atrial than ventricular junctophilin-2 expression and further downregulated after TAC, we hypothesized that JP2-OE may exert functional and, ultimately, disease-mitigating effects in atrial cardiomyopathy. As JP2-OE in the ventricles directly driven by the mouse αMHC promotor was previously established (15), we analyzed atrial tissue in JP2-OE mice, confirming an approximately 5-fold increased junctophilin-2 protein expression compared with WT mice

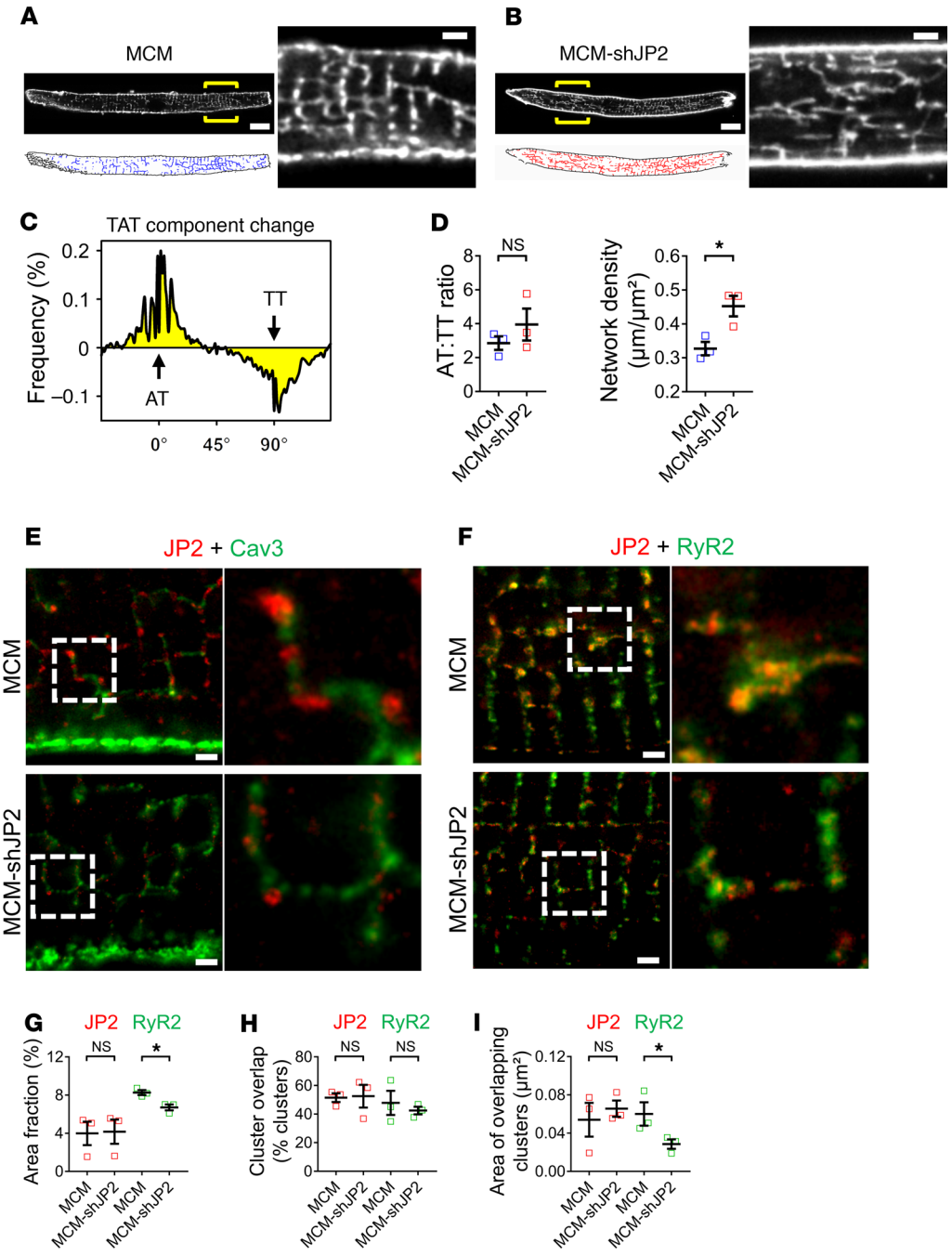


**Figure 5. Atrial Junctophilin-2 knockdown induces tubular network proliferation and disrupts AT-SR junctional membrane complexes.** Confocal live-membrane imaging (di-8-ANEPPS) in AMs isolated from (**A**) control (MCM) and (**B**) junctophilin-2–knockdown (JP2-knockdown) hearts (MCM-shJP2). Yellow brackets indicate magnified regions. Scale bars: 10 μm (whole cell); 2 μm (magnification). TAT network skeletons (bottom) were extracted for MCM (blue) versus MCM-shJP2 (red) analysis. (**C**) Frequency histogram subtraction (MCM-shJP2 minus MCM) revealed increased AT (0°) versus decreased TT (90°) components. (**D**) Dot plots summarizing AT/TT ratio and TAT network density after MCM-shJP2 knockdown. *n* = 3 individual hearts each for 56 MCM and 56 MCM-shJP2 AM cells. Dual-color STED imaging of JP2 and (**E**) caveolin-3 or (**F**) RyR2. Magnified views (right) show apparent JP2 and RyR2 cluster changes caused by MCM-shJP2 knockdown. Scale bars: 1 μm. (**G**–**I**) Dot plots summarizing MCM-shJP2 knockdown changes: (**G**) a decreased RyR2 area fraction; (**H**) an unchanged overlap between RyR2 and JP2 clusters; and (**I**) a significantly decreased area of RyR2 clusters overlapping with JP2 clusters. *n* = 3 individual hearts each for 30 MCM and 22 MCM-shJP2 AM cells. **P* < 0.05, Student's *t* test.

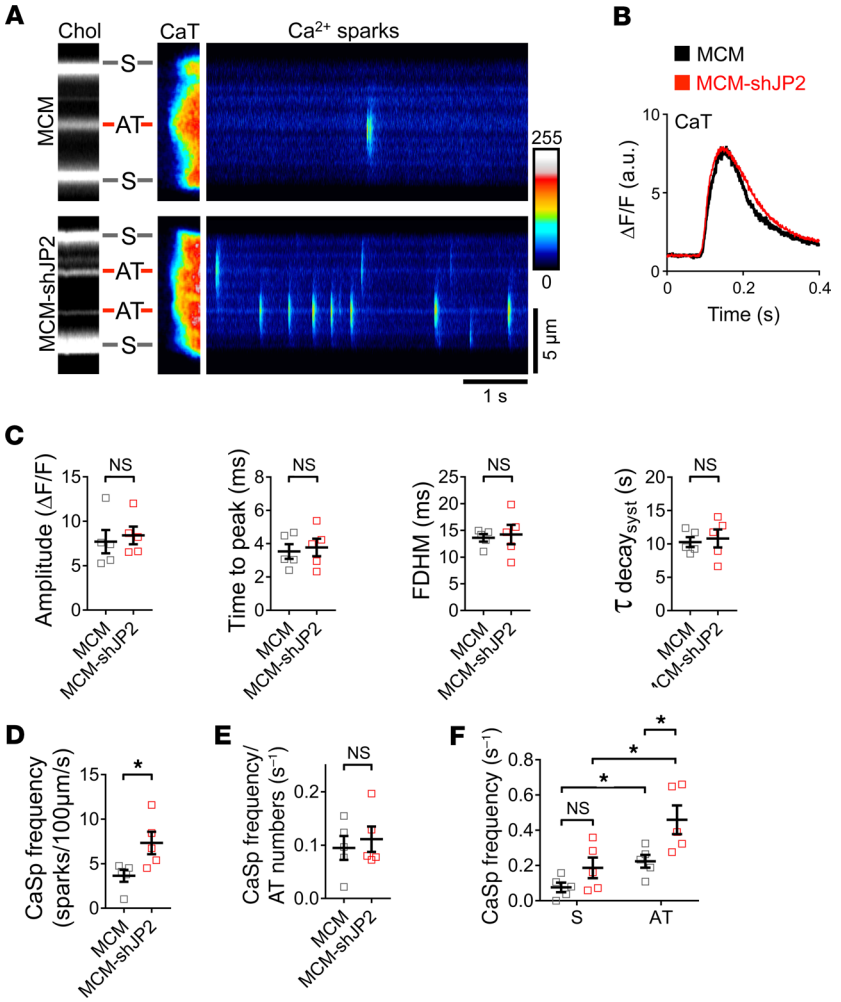


**Figure 6. Junctophilin-2 knockdown increases $Ca^{2+}$ leak in atrial myocytes.** (**A**) Combined live-cell membrane (Cholesterol-PEG-KK114, Chol) and intracellular $Ca^{2+}$ (fluo-4 AM) imaging in intact AMs. Shown are the final $Ca^{2+}$ transients (CaT) followed by spontaneous $Ca^{2+}$ sparks after 1-Hz pacing (5 times field stimulation). Note earlier $Ca^{2+}$ release from AT sites compared with subsurface (S) sites. $Ca^{2+}$ sparks occurred more frequently at AT sites after MCM-shJP2 knockdown. (**B**) Exemplar $Ca^{2+}$ transient traces and (**C**) quantitative parametric analysis showed no significant differences between MCM and MCM-shJP2 knockdown. *n* = 5 individual hearts each for 19 MCM and 16 MCM-shJP2 AM cells. (**D**) Dot plot showing a significant increase in $Ca^{2+}$ spark (CaSp) frequency in MCM-shJP2 cells. (**E**) In contrast, the AT-normalized $Ca^{2+}$ spark frequency was not significantly changed after MCM-shJP2 knockdown. (**F**) $Ca^{2+}$ spark frequency is increased at AT sites. *n* = 5 individual hearts each for 22 MCM and 20 MCM-shJP2 AM cells in **D** and **F**. **P* < 0.05, Student's *t* test.

(Figure 7, A and B, and Supplemental Figure 1). Interestingly, both RyR2 expression and phosphorylation at Ser2808 were increased by approximately 40%, indicating a higher capacity for junctional $Ca^{2+}$ release (Figure 7B). While caveolin-3, phospholamban, SERCA2a, and the atria-specific $Ca_V1.3$ channel were not changed (Figure 7, C and E), expression of the $Ca_V1.2$ channel and the $Na^+/Ca^{2+}$ exchanger were both significantly increased in JP2-OE atria (Figure 7, D and E). Finally, echocardiography confirmed a normal left atrial structure and function at baseline in JP2-OE mice versus WT mice (Supplemental Figure 7).

*JP2-OE augments AT-SR junctional RyR2 clustering.* AMs from WT and JP2-OE mice were isolated to image the intact TAT membrane network in living cells (Figure 8, A and B). While cell length was mildly increased, cell width and the length-to-width ratio of JP2-OE AMs were unchanged (Supplemental Figure 8). Whereas TAT analysis documented both a normal AT/TT component ratio and TAT network density (Figure 8C), atrial JP2-OE cells showed numerous large intracellular de novo membrane structures of (sub)micrometer size (Figure 9B). To characterize these membrane organelles in intact AMs, we used Cholesterol-PEG-KK114 (5 µM) bulk staining for live-STED superresolution microscopy (21), resolving stacked tubule components tightly packed inside larger membrane superstructures in JP2-OE cells but

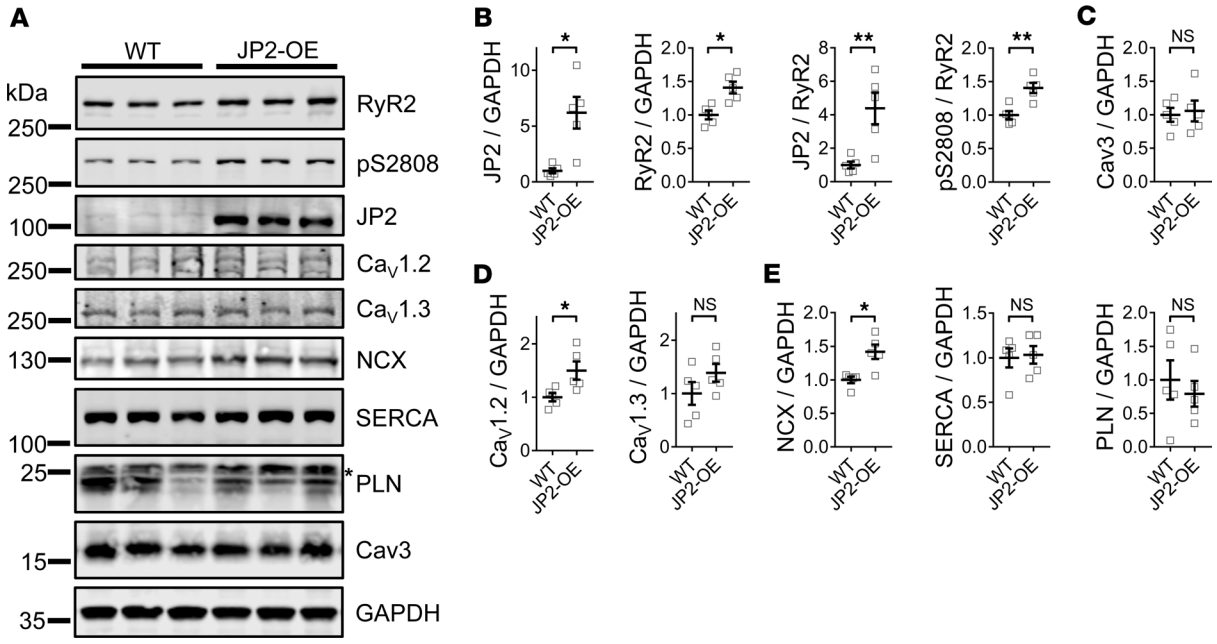


**Figure 7. Transgenic junctophilin-2 overexpression increases RyR2, $Ca_V1.2$, and NCX1 protein expression.** (**A**) Representative immunoblots from WT and junctophilin-2–overexpressing (JP2-overexpressing [JP2-OE]) mouse atrial tissue lysates. Dot plots summarize (**B**) increased JP2 and RyR2 protein and RyR2-pS2808 phosphorylation levels, the latter indicating a higher capacity for atrial $Ca^{2+}$ release; (**C**) unchanged expression of caveolin-3; (**D**) significantly increased expression of the L-type $Ca^{2+}$ channel isoform $Ca_V1.2$ versus unchanged $Ca_V1.3$ protein; and (**E**) increased NCX1 versus unchanged SERCA2a and PLN expression. Representative data from 3 independent experiments. $n$ = 5 WT and 5 JP2-OE atria. $^*P < 0.05$; $^{**}P < 0.01$, Student's $t$ test.

not in WT cells (Figure 8D). Apparently, these superstructures were continuous with freestanding AT components, as Cholesterol-PEG-KK114 diffused unhindered via the outer membrane leaflet into and throughout the locally stacked membrane superstructures (Figure 8D). In addition to a variety of complex AT-connected superstructures (Supplemental Figure 9A), smaller stacks composed of only 2 quasi-parallel tubules were also observed (Supplemental Figure 9B). Quantitatively, using AT cross-sectional signal profiling, we found an unchanged mean AT diameter (full width of half maximum [FWHM]) in atrial WT cells versus JP2-OE cells, together with stacked superstructures in JP2-OE cells on average approximately 3 times larger compared with AT diameters (Figure 8E).

ET of semi-thick sections resolved the 3D membrane architecture of tubule-stacked superstructures in JP2-OE cells (Figure 8F; tubules, green; SR, yellow). Strikingly, inside each superstructure, multiplexed junctions between AT-connected tubule components and SR membranes occurred from more than one side (Figure 8F, Supplemental Video 1, and Supplemental Figure 9C). Moreover, these "polyadic" AT-SR junctions appeared to be densely filled with RyR2 channels in JP2-OE cells, apparently on opposite sides of junctional SR structures and, hence, each intercalating the tubule stacks from 2 sides (Figure 8F and Supplemental Figure 9C).

Next, to confirm the identity and distribution of key junctional membrane proteins inside tubule superstructures, we applied dual-color STED microscopy. Costaining of caveolin-3 identified ATs with extensive junctional junctophilin-2 clusters in JP2-OE cells and clearly beyond the size of junctophilin-2 clusters apparent in WT AMs (Figure 8G). In addition, coimmunolabeling identified more extensive junctional RyR2 clustering substantially overlapping with junctophilin-2 clusters in JP2-OE cells (Figure 8H). Importantly, larger junctional RyR2 clusters in JP2-OE cells were highly phosphorylated at Ser2808 (Figure 8I). Image analysis confirmed both significantly increased area fraction and dimensions of overlapping junctophilin-2 clusters, along with an increased size of overlapping RyR2 clusters in JP2-OE compared with WT AMs (Figure 8, J and K). However, in contrast to dyadic AT-SR junctions described in WT AMs previously (12), magnified ET images of AT-connected tubule components inside individual superstructures in JP2-OE AMs not only confirm the dense polyadic organization of AT-SR junctions but support extensive electron-dense RyR2 channel clustering (Figure 8L). Thus, JP2-OE induced the formation of polyadic AT-SR junctions inside stacked tubule superstructures greatly augmenting local junctophilin-2 and RyR2 coclustering.

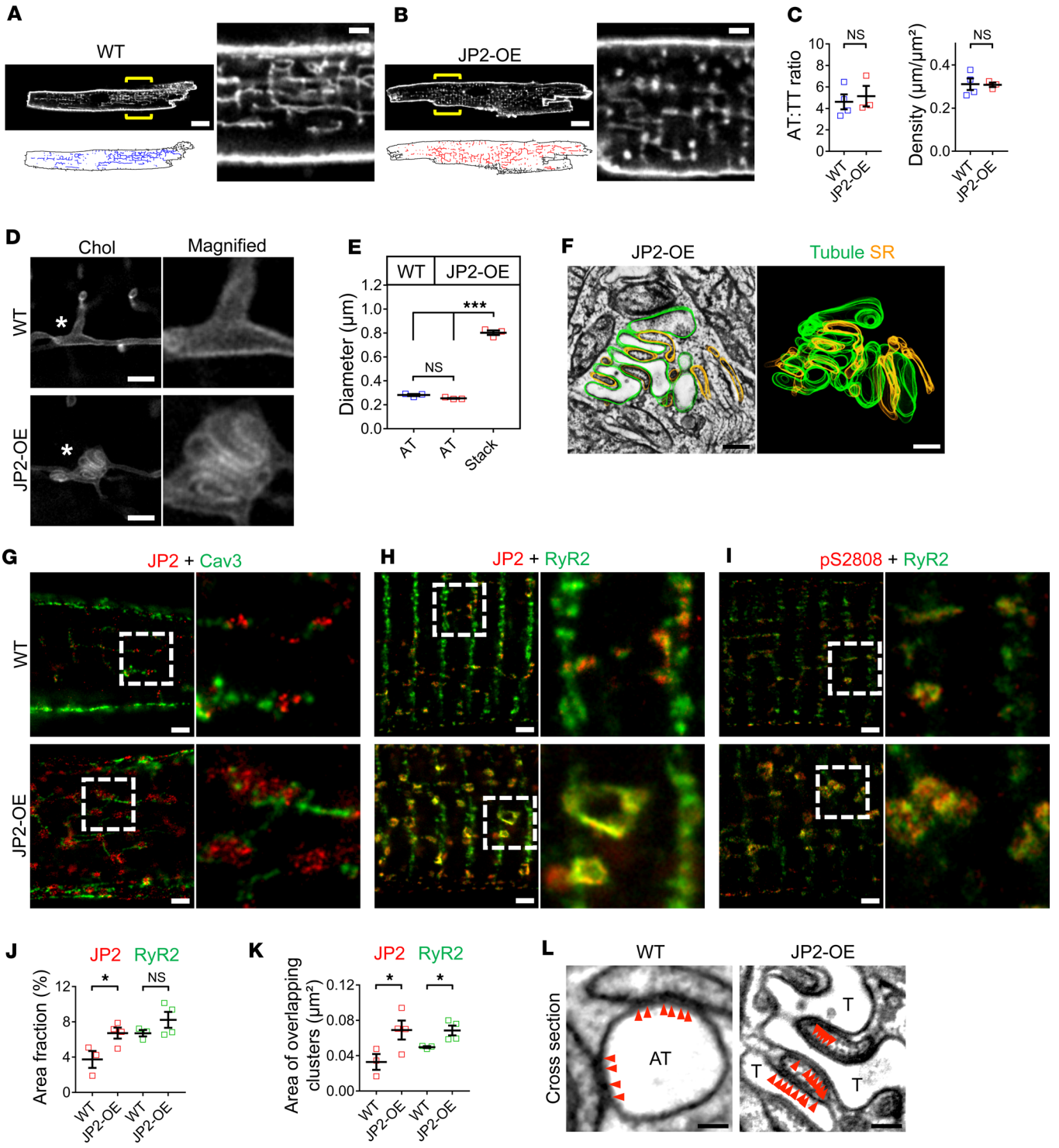


**Figure 8. Junctophilin-2 overexpression increases RyR2 clustering through de novo biogenesis of polyadic AT-SR junctional membrane complexes.** Confocal live imaging (di-8-ANEPPS) in AMs from (**A**) WT versus (**B**) JP2-OE hearts. Yellow brackets indicate magnified AM regions. Scale bar: 10 μm (whole cell); 2 μm (magnification). (**C**) TAT network skeleton (**A** and **B**, bottom left) analysis. Dot plots summarizing the network density and the AT/TT component ratio. *n* = 3 individual hearts each for 34 WT and 32 JP2-OE AM cells. (**D**) Live STED nanoscopy of Cholesterol-PEG-KK114–stained (Chol-stained) AMs showed AT-associated stacked tubule superstructures in JP2-OE. Asterisks identify magnified structures. Scale bar: 1 μm. (**E**) Dot plot summarizing AT diameters in WT versus JP2-OE cells and stacked tubule superstructure dimensions in JP2-OE cells. *n* = 3 individual hearts each; 34 ATs from 22 WT versus 38 ATs from 23 JP2-OE AM cells; and 15 tubule superstructures from JP2-OE AMs. (**F**) Representative ET 3D reconstruction of a tubule superstructure in JP2-OE AMs. Note the complex 3D tubule organization (green) and multiplexed polyadic junctional contacts with SR membranes (yellow). Scale bar: 200 nm. (**G**–**I**) Dual-color STED IF imaging of AMs from WT versus JP2-OE mice of junctophilin-2 (JP2) and (**G**) caveolin-3 or (**H**) RyR2 and (**I**) RyR2-pS2808 and RyR2. AMs from JP2-OE hearts show (**G**) strongly increased JP2 clustering at caveolin-3–labeled AT structures; (**H**) JP2 cluster colocalization with large RyR2 clusters; and (**I**) increased highly Ser2808-phosphorylated RyR2 cluster areas. Dashed

boxes indicate magnified regions. Scale bars: 1 μm. (**J** and **K**) Dot plots showing analysis of segmented STED images: (**J**) JP2 area fraction and (**K**) overlapping JP2 and RyR2 clusters are significantly increased in JP2-OE cells. $n$ = 3 WT and 4 JP2-OE hearts for 17 WT and 24 JP2-OE AM cells. (**L**) ET images comparing AT-SR junctions of cross-sectioned AT structure (left) versus stacked tubule superstructures (T, right) in different AMs as indicated. Arrowheads mark electron-dense RyR2 channels. Scale bar: 100 nm. *$P$ < 0.05; ***$P$ < 0.001, Student's $t$ test, except in **E**, in which 1-way ANOVA was used.

*$Ca_V1.2$ channel expression in atrial JP2-OE cells*. As voltage-dependent L-type $Ca^{2+}$ channels are essential to activate CICR in AMs, we wondered if polyadic AT-SR junctions with enhanced RyR2 clustering due to JP2-OE additionally recruit $Ca_V1.2$ channels. As compared with WT cells, AMs isolated from JP2-OE hearts apparently express greater numbers of $Ca_V1.2$ clusters organized in large junctional structures at caveolin-3–labeled membrane domains at AT structures (Figure 9A), and $Ca_V1.2$ clusters colocalize with junctophilin-2 signals (Supplemental Figure 10). Image analysis of the $Ca_V1.2$ cluster area confirmed a significant increase at AT structures inside AMs from JP2-OE versus WT hearts (Figure 9B). Finally, coimmunoprecipitation experiments confirmed a direct interaction between junctophilin-2 and $Ca_V1.2$ in WT mouse heart lysates as reported previously (Figure 9C, Supplemental Figure 1, and ref. 26). These data support the notion that increased junctophilin-2 and RyR2 expression in polyadic AT-SR junctions augments CICR through additional recruitment of $Ca_V1.2$ channels.

*JP2-OE increases global and local $Ca^{2+}$ release*. We hypothesized that polyadic RyR2 clustering inside junctional tubule superstructures amplifies and compartmentalizes local $Ca^{2+}$ release in JP2-OE AMs. Combining transversal $Ca^{2+}$ transient profiling with membrane imaging, we recorded pacing-evoked and spontaneous $Ca^{2+}$ release signals at AT and subsurface sites in JP2-OE cells (Figure 10A). During 1-Hz pacing, spatially averaged $Ca^{2+}$ transients peaked at a higher level in JP2-OE compared with WT cells, while the peak of caffeine-stimulated SR $Ca^{2+}$ release was similar (Figure 10B). Average $Ca^{2+}$ transient analysis confirmed a significant amplitude increase, whereas time to peak, duration (FDHM), and decay (τ) were not significantly changed in JP2-OE AMs (Figure 10C). Whereas SR $Ca^{2+}$ load was not changed, the caffeine-induced $Ca^{2+}$ decay kinetics (τ) were significantly accelerated (Figure 10D), consistent with increased $Na^+/Ca^{2+}$ exchanger expression (Figure 7, A and E). Presumably, elevated $Na^+/Ca^{2+}$ exchange compensates increased $Ca^{2+}$ influx via increased junctional $Ca_V1.2$ clustering in JP2-OE cells (Figure 9, A and B).

Notably, following 1-Hz pacing, $Ca^{2+}$ sparks occurred more frequently at AT sites from JP2-OE cells compared with WT AMs (Figure 10A). Quantitative analysis confirmed a globally increased $Ca^{2+}$ spark frequency in JP2-OE AMs (Figure 10E). In contrast to atrial junctophilin-2 knockdown, however, the increase in $Ca^{2+}$ sparks in JP2-OE AMs was not associated with any numerical AT proliferation (Figure 10F). Yet, $Ca^{2+}$ sparks originating from ATs were approximately 2 times more frequent in JP2-OE compared with WT cells and also significantly increased compared with JP2-OE subsurface membrane sites (Figure 10G). Hence, junctional $Ca^{2+}$ release is increased at AT membrane structures deep inside AMs overexpressing junctophilin-2.

*JP2-OE attenuates atrial dysfunction and mortality*. Important for unbiased in vivo analysis, induction of junctophilin-2 knockdown was associated with 0 mortality for up to 4 weeks after tamoxifen treatment (Figure 11A). However, if junctophilin-2 knockdown was induced 3 days after TAC, 100% mortality occurred within 20 days as compared with 40% mortality within 28 days in MCM control mice (Figure 11B). Interestingly, 2 weeks after TAC (11 days after tamoxifen treatment) both atrial and ventricular histology sections showed no apparent differences in cardiomyocyte hypertrophy or interstitial fibrosis between MCM and MCM-shJP2 hearts (Supplemental Figure 11), while the potential for profound left atrial AM hypertrophy 4 weeks after TAC in WT mice was shown previously (12). Thus, excess mortality after TAC in junctophilin-2–knockdown animals may be attributed at least in part to junctophilin-2 downregulation and aggravated heart failure.

If atrial junctophilin-2 downregulation contributes to heart failure mortality, JP2-OE may improve survival. Strikingly, the entire group of JP2-OE mice survived 28 days after TAC, in contrast with significant mortality observed for every fourth WT control animal (Figure 11C). We excluded significant differences between the transaortic gradient and body weight after TAC between WT and JP2-OE mice; however, the heart-to-body-weight ratio was significantly decreased in JP2-OE mice (Figure 11D). While echocardiography showed a nonsignificant trend toward a smaller left atrial diameter in JP2-OE mice 4 weeks after TAC, it revealed a profound increase in left atrial fractional shortening compared with WT control mice (Figure 11E), an improvement clearly beyond the extent of mildly improved left ventricular function in JP2-OE mice (Figure 11F), the latter comparable to an earlier study (25). Finally, histological sections revealed a substantially reduced left atrial interstitial fibrosis, in addition to left

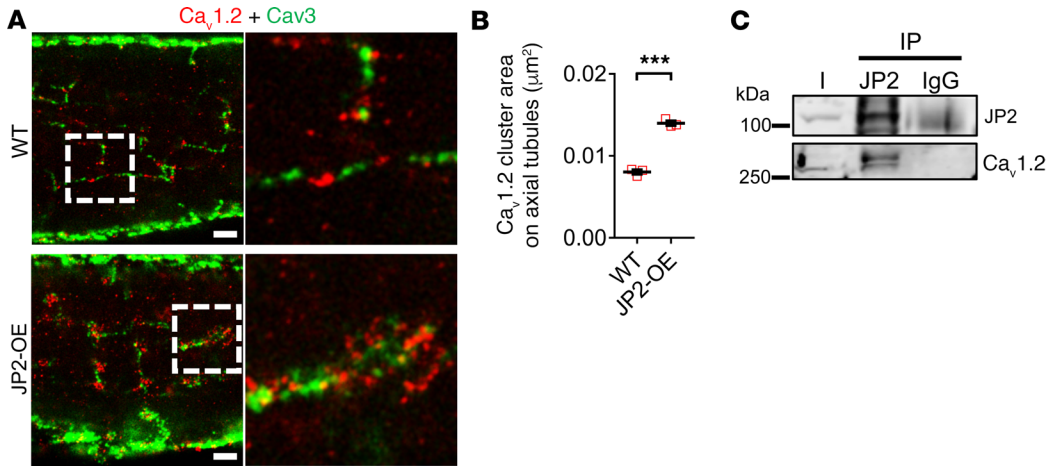


**Figure 9. Expression of the L-type $Ca^{2+}$ channel $Ca_V1.2$ in polyadic junctional membrane complexes in atrial JP2-OE cells and interaction with junctophilin-2.** (**A**) Dual-color STED IF imaging of $Ca_V1.2$ and caveolin-3 in AMs from WT versus JP2-OE mouse hearts. Dashed boxes indicate magnified regions. Scale bars: 1 μm. (**B**) Dot plot summarizing the mean $Ca_V1.2$ cluster area at axial tubule components analyzed by STED image segmentation. AMs from JP2-OE hearts show a strong increase in $Ca_V1.2$ clustering at caveolin-3–labeled AT structures. $n = 3$ individual hearts each for 8 WT and 8 JP2-OE AM cells. $^{***}P < 0.001$, Student's $t$ test. (**C**) Junctophilin-2 immunoprecipitation. Western blotting confirmed the protein-protein interaction between junctophilin-2 (JP2) and $Ca_V1.2$ in WT mouse heart lysate. I, input; IgG, negative control.

ventricular fibrosis, in JP2-OE compared with WT hearts 4 weeks after TAC (Supplemental Figure 12). Taken together, JP2-OE significantly decreased mortality, at least in part through greatly improved left atrial function and diminished left atrial fibrosis after TAC.

For subcellular TAT network analysis, we imaged left AMs from WT and JP2-OE hearts 4 weeks after TAC. While no significant difference in TAT network density and AT/TT ratio were apparent (Figure 11G), notably, large tubule-stacked superstructures were preserved in JP2-OE cells (Figure 11H). Dual-color STED imaging confirmed extensive junctophilin-2 clustering at caveolin-3–labeled AT-SR junctions in left atrial JP2-OE cells after TAC (Figure 11I). In JP2-OE cells, junctophilin-2 clusters overlapped robustly with large RyR2 clusters, in contrast with markedly decreased RyR2 clustering in WT cells after TAC (Figure 11J). Moreover, junctional RyR2 clusters in JP2-OE cells were highly phosphorylated at Ser2808 (Figure 11K). Finally, 4 weeks after TAC, left atrial cell dimensions were significantly smaller in JP2-OE cells (Figure 11L) and sarcomere shortening was significantly increased compared with WT cells (Figure 11M). Notably, both the amplitude and maximal velocity ($V_{max}$) of sarcomere shortening were nearly doubled in JP2-OE cells compared with WT cells 4 weeks after TAC (Figure 11M), consistent with robustly increased left atrial shortening in vivo (Figure 11E). In summary, JP2-OE prevented the TAC-induced disruption of left atrial JMCs, adverse tissue remodeling, contractile dysfunction, and contributed to a greatly diminished mortality rate.

## Discussion

We identified what we believe to be previously unknown atrial mechanisms of differential subcellular junctophilin-2 clustering, RyR2 cluster disruption in JMCs, and transgenic correction of atrial dysfunction characterized by (a) approximately 5-fold lower atrial versus ventricular junctophilin-2 protein expression, resulting in a constitutively decreased junctophilin-2/RyR2 ratio in mouse and human atria. (b) Additionally, large junctophilin-2 clusters at AT-SR junctions stabilize extensive RyR2 co-clustering in AMs. (c) In contrast, pressure overload induced a profound reorganization of AT structures in human and mouse atria, together with decreased junctophilin-2 and RyR2 protein expression, contributing to contractile dysfunction and paroxysmal arrhythmia susceptibility. In contrast, (d) JP2-OE preserved and augmented junctional RyR2 clustering through biogenesis of polyadic superstructures, inhibiting adverse left atrial tissue remodeling and diminishing mortality at least in part through significantly improved atrial contractile function. Together, these observations support a potentially new therapeutic rationale based on biomimetic augmentation of atrial function through increased junctophilin-2 expression to prevent disruption of atrial JMCs due to pressure overload, adverse cardiac remodeling, and deterioration of heart failure.

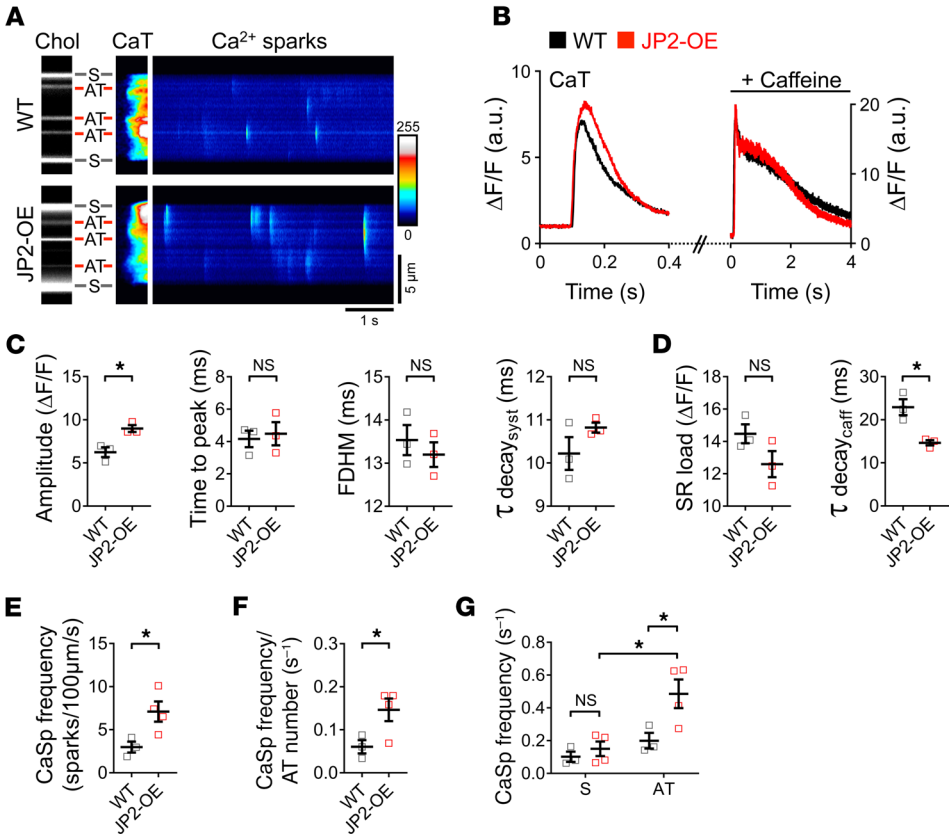


**Figure 10. Increased $Ca^{2+}$ release in atrial myocytes overexpressing junctophilin-2.** (**A**) Combined live membrane (Cholesterol-PEG-KK114 [Chol]) and $Ca^{2+}$ (fluo-4 AM) imaging in intact WT and JP2-OE AMs. The final $Ca^{2+}$ transient (CaT) at 1-Hz pacing is followed by spontaneous $Ca^{2+}$ sparks. Transverse line scanning shows that the $Ca^{2+}$ release occurs earlier at AT sites, followed by AM subsurface (S) sites. Note larger repetitive $Ca^{2+}$ sparks firing at AT sites in JP2-OE. (**B–D**) Exemplar systolic and caffeine-induced $Ca^{2+}$ transient traces and quantitative analysis: JP2-OE AMs show increased $Ca^{2+}$ transient amplitude (**C**) consistent with increased $Ca_V1.2$, RyR2, and RyR2-pS2808 expression and significantly faster decay of caffeine-induced $Ca^{2+}$ release (**D**), indicating higher NCX function. *n* = 3 individual hearts each for 16 WT versus 12 JP2-OE AM cells (**C**) and 20 WT versus 17 JP2-OE AMs (**D**). (**E**) Dot plots summarizing a significantly increased $Ca^{2+}$ spark (CaSp) frequency in JP2-OE cells and (**F**) a significant increase in $Ca^{2+}$ spark frequency per AT. *n* = 3 WT and 4 JP2-OE hearts for 15 WT and 15 JP2-OE AM cells. (**G**) $Ca^{2+}$ spark frequency at subsurface (S) versus AT sites in JP2-OE cells. *n* = 3 WT and 4 JP2-OE individual hearts for 15 WT and 15 JP2-OE AMs cells. *$P < 0.05$, Student's *t* test.

Here, pressure overload induced a profound reorganization of AT structures in human and mouse atria together with decreased junctophilin-2 protein expression and RyR2 cluster disruption. Whereas AT proliferation was clearly evidenced at the network and local ultrastructural level 4 weeks after TAC in mice, in human atrial myocardium with chronic aortic valve stenosis subcellular AT fragmentation and loss of junctophilin-2 clustering were observed. While atrial shRNA-JP2 knockdown was sufficient to cause contractile dysfunction and AT proliferation, RyR2 cluster disruption, and increased $Ca^{2+}$ leak, remarkably this occurred without any hypertrophic or fibrotic remodeling. Taken together, AMs are clearly susceptible to contractile dysfunction induced by junctophilin-2 downregulation and AT proliferation following pressure overload. Notably, within this context, both new preclinical models and diagnostic strategies to identify atrial dysfunction earlier are urgently needed for therapeutic translation: (a) hypertension was estimated to represent a leading risk factor of atrial dysfunction in 60%–80% of European patients (27) and (b) calcific aortic valve stenosis has lately increased in prevalence to 1.7% in the general population older than 65 years (28).

Recently, a "super-hub" signaling mechanism of relevance for atrial health and disease, including arrhythmia substrates and depressed contractility, was identified. Compared with sparse TTs in AMs, abundant AT-SR structures with significantly larger surface areas and extensive dyadic junctions were documented (12). Notably, atrial AT-SR junctions contain 2 voltage-dependent L-type $Ca_V1.2$ and $Ca_V1.3$ channels (21) and highly phosphorylated RyR2 channels, each with unique regulatory properties, while hypertrophic

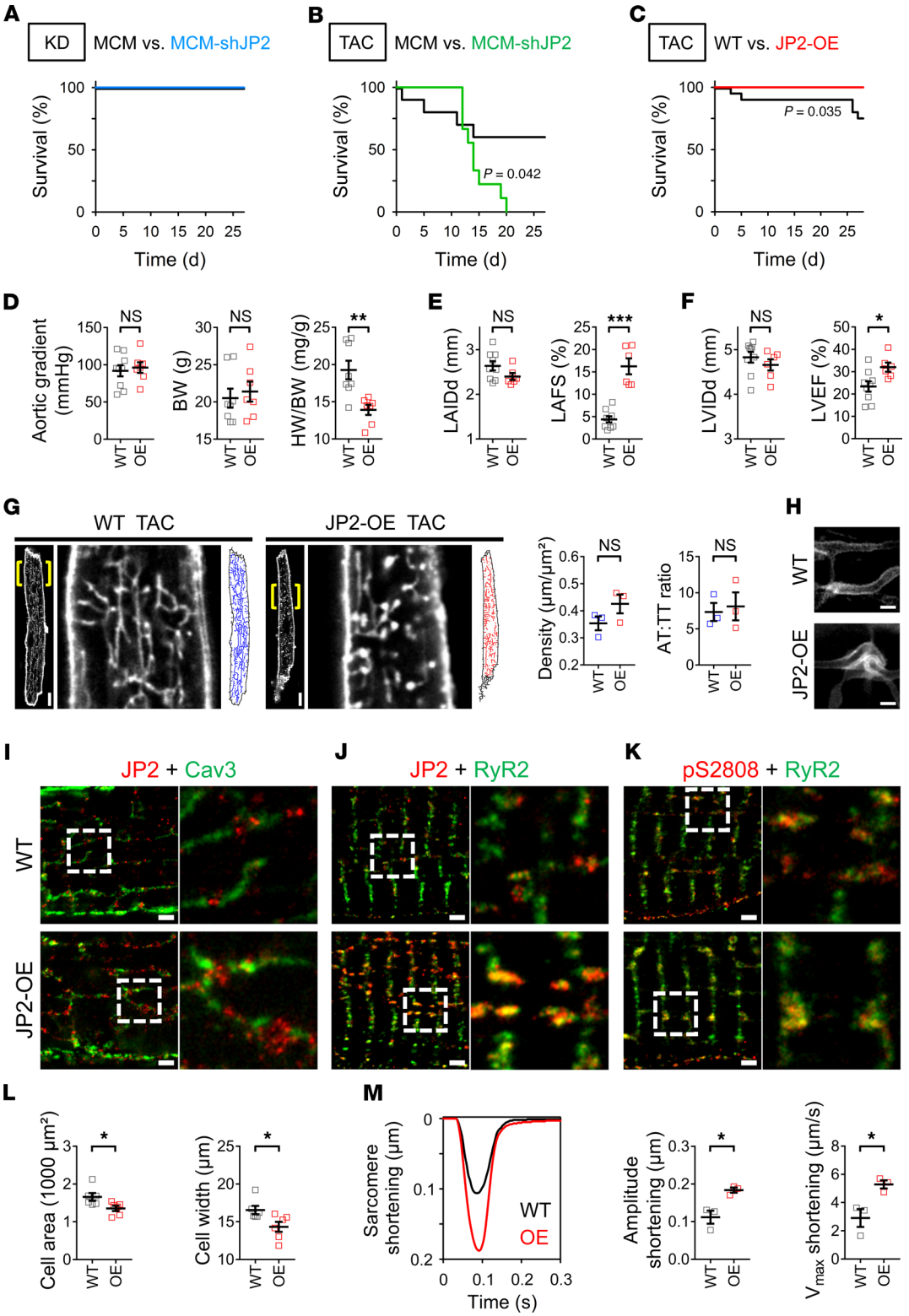


**Figure 11. Junctophilin-2 overexpression attenuates atrial loss of function after TAC.** (**A**) Survival analysis showed no increase in mortality after junctophilin-2 (JP2) knockdown ($n$ = 7 MCM versus 7 MCM-shJP2 mice). (**B**) After TAC mortality reached 100% within 20 days ($n$ = 10 MCM versus 9 MCM-shJP2 mice). (**C**) In contrast, 100% of JP2-OE mice survived 4 weeks after TAC surgery, whereas 25% of WT control animals died ($n$ = 20 WT versus 16 JP2-OE mice). (**D**) Dot plots showing similar trans-aortic gradients (9 WT, 7 JP2-OE mice) but a decreased heart-to-body-weight ratio (HW/BW) in JP2-OE mice ($n$ = 8 WT, 7 JP2-OE mice). (**E** and **F**) Dot plots summarizing echocardiographic left atrial (LA) and left ventricular (LV) diastolic dimensions, strongly increased LA fractional shortening (FS), and moderately improved LV ejection fraction (EF) in JP2-OE mice after TAC. $n$ = 9 WT and 7 JP2-OE mice. (**G**) Confocal live-membrane imaging (Cholesterol-PEG-KK114) of left atrial WT and JP2-OE cells after TAC showed no differences in TAT network density and AT/TT component ratio. Yellow brackets indicate magnified views. Scale bar: 10 μm. $n$ = 3 individual hearts each for 32

WT and 24 JP2-OE AM cells. (**H**) Live-membrane STED nanoscopy (Cholesterol-PEG-KK114) shows preserved tubule superstructures in JP2-OE cells after TAC. Scale bar: 500 nm. (**I**–**K**) Dual-color STED nanoscopy after TAC for JP2 and (**I**) caveolin-3 or (**J**) RyR2 and (**K**) RyR2-pS2808 and RyR2. After TAC, JP2-OE cells showed larger and highly phosphorylated RyR2 clusters at caveolin-3–labeled tubular structures. Dashed boxes indicate magnified regions. Scale bar: 1 μm. (**L**) Dot plots showing decreased cell area and width for JP2-OE after TAC. $n$ = 6 individual hearts each for 44 WT versus 36 JP2-OE AM cells. (**M**) Single-cell sarcomere shortening traces of left atrial myocytes after TAC. Dot plots summarizing significantly improved shortening amplitude and maximal velocity ($V_{max}$) in JP2-OE cells. $n$ = 3 individual hearts each for 33 WT versus 30 JP2-OE AM cells. *$P$ < 0.05; **$P$ < 0.01; ***$P$ < 0.001, Mantel-Cox test (**A**–**C**); Student's $t$ test (**D**–**G** and **L** and **M**).

remodeling was shown to diminish the physiological latency profile between AT-SR junctional and non-junctional $Ca^{2+}$ release (12). It is well established that atrial fibrillation can induce a downregulation of the L-type $Ca^{2+}$ current and chronic loss of contractile function (7). Interestingly, JP2-OE resulted in increased atrial $Ca_V1.2$ protein levels and increased $Ca_V1.2$ channel clustering at AT-SR junctions, while contractile function was greatly improved after TAC. STED and ET imaging showed extensive AT-associated protein clustering in JMCs, indicating a prominent role in atrial excitation-contraction coupling based on large highly phosphorylated, as opposed to disrupted smaller RyR2 clusters after TAC or shRNA-mediated knockdown. Hence, junctophilin-2 clustering has an essential role in unusually large atrial AT-SR junctions, where a higher local concentration of N-terminal MORN domains can provide high affinity noncovalent binding of charged phospholipids (14), stabilizing the junctional contact with the AT membrane. Thus, our observations about junctophilin-2 clustering at ATs in health versus disease identify unique atrial mechanisms, significantly extending the emerging model of atrial super-hub $Ca^{2+}$ signaling (12).

Importantly, junctophilin-2 downregulation in hypertrophied AMs may reach critically low levels, approximately one order of magnitude below healthy VMs, profoundly disrupting coclustering with RyR2 channels at AT-SR junctions. While human and mouse VMs expressed significantly higher junctophilin-2 levels (Figures 1 and 2), our data in AMs generally support the concept that junctophilin-2 is essential for maturation and function of JMCs (29, 30). In AMs, however, decreased junctophilin-2 expression both after TAC and after knockdown was associated with numerical and local AT proliferation characterized by structurally and functionally disrupted AT-SR junctions. Recently, Guo et al. identified an additional nonstructural role: nuclear translocation of an N-terminal junctophilin-2 peptide (JP2NT) was shown to regulate transcription in VMs (31). Considering the caveat that JP2NT has not been studied in AMs, the subcellular and stoichiometric JP2 protein expression and cleavage mechanisms might differ fundamentally from VMs. Mechanistically, decreased junctophilin-2 clustering disrupted the AM-specific ultrastructure and function of AT-SR junctions, while JP2-OE rescued atrial function and diminished heart failure mortality. Based on the immediate biomedical relevance of disrupted versus restored junctophilin-2 clustering for the function of the atrial booster-pump during active ventricular filling, we propose that transgenic correction of junctophilin-2 expression merits future evaluation as a biomimetic therapeutic intervention, particularly in the disease context of combined atrial dysfunction and heart failure.

Prior studies revealed that alterations in the junctophilin-2/RyR2 stoichiometry can lead to atrial fibrillation. A genetic mutation in junctophilin-2 (E169K), disrupting RyR2 binding, causes atrial arrhythmias in patients with hypertrophic cardiomyopathy with this mutation (18). Similar findings were obtained in knockin mice with the same E169K mutation, reducing junctophilin-2 mediated binding to and stabilization of RyR2, thereby promoting abnormal SR $Ca^{2+}$ release events and $Ca^{2+}$ leak in AMs from E169K knockin mice (18). Furthermore, atrial fibrillation inducibility was increased in junctophilin-2–knockdown mice (18). Whereas patients with paroxysmal atrial fibrillation were found to have increased total RyR2 protein levels, junctophilin-2 levels were similar to patients in sinus rhythm, resulting in a reduced junctophilin-2/RyR2 ratio (18, 32). In isolated AMs from paroxysmal atrial fibrillation patients, an increased incidence of proarrhythmic $Ca^{2+}$ release events was confirmed (32). Thus, junctophilin-2 plays a critical role in stabilizing RyR2 in AMs, while a decreased junctophilin-2/RyR2 ratio can promote aberrant $Ca^{2+}$ handling and atrial fibrillation. JP2-OE, which significantly enhanced local $Ca^{2+}$ release and atrial contractility, appears to be a viable concept to correct a decreased junctophilin-2/RyR2 ratio. As JP2-OE after TAC diminished adverse atrial remodeling and mortality, which are frequently encountered in patients with atrial fibrillation and heart failure, transgenic viral vector interventions seem promising to prevent atrial dysfunction and heart failure decompensation.

Notably, skeletal muscle $Ca_V1.1$ and RyR1 channels are clustered in triad junctions, where TTs are closely juxtaposed by 2 terminal SR cisternae (33, 34). In cardiac muscle, however, junctional SR cisternae adjoin TTs in dyads from only one side (25, 35). Both dyads and triads are collectively referred to as JMCs.

While transgenic JP2-OE led to a significantly increased dyadic frequency and junctional coupling area in VMs, neither ventricular function nor the $Ca^{2+}$ transient amplitude or $Ca^{2+}$ spark frequency were enhanced previously (25). In contrast, atrial JP2-OE significantly increased the $Ca^{2+}$ transient amplitude and the frequency of $Ca^{2+}$ sparks at AT-SR junctions (Figure 10). However, the mouse model described by Guo et al. differs markedly; it is based on a modified αMHC promoter with an additional tet-operon, which results in less junctophilin-2 expression compared with our model (25); additionally, it has a C57BL/6J genetic background, which is devoid of the mitochondrial transhydrogenase recently shown to ameliorate pressure overload–induced heart failure in mice (36). While ventricular JP2-OE resulted in few "convoluted" TT structures with junctional dyads (25), atrial JP2-OE induced de novo polyadic AT-SR junctional superstructures verified by live-cell STED nanoscopy and ET 3D reconstruction (Figure 8). Taken together, to our best knowledge, this represents the first demonstration of a potentially therapeutic mechanism of densely tubule-stacked junctional superstructures, namely polyadic junctions on ATs, improving cardiomyocyte function in normal atria and after TAC.

We and others have provided evidence that ventricular junctophilin-2 expression is decreased in animal models and human heart failure, contributing to excitation-contraction uncoupling through loss of ultrastructural dyadic integrity (17, 37–40). During increased cardiac stress junctophilin-2 can be proteolytically cleaved by calpain (41, 42) or downregulated by miR-24 (38). Remarkably, we found that atrial compared with ventricular junctophilin-2 protein levels in human and mouse hearts were approximately 5-fold lower at baseline and, thus, already below maximally depressed ventricular junctophilin-2 levels found in heart failure or after shRNA-mediated knockdown. While downregulation of junctophilin-2 was not studied in human atria previously, we propose that a critically decreased junctophilin-2/RyR2 ratio may render the more rapidly contracting human atria prone for junctional disruption and loss of function.

While atrial fibrillation and heart failure together result in significantly increased mortality, existing therapies — developed for either syndrome alone — fail more frequently in patients with this adverse disease combination (1–4). This emphasizes an urgent need for new strategies to treat and/or prevent latent and symptomatic forms of atrioventricular dysfunction. Studies showed that cardiomyocyte-specific JP2-OE may protect the left ventricle from maladaptive remodeling in mouse models of heart failure (15, 18, 30). In addition, we identify atria-specific junctional uncoupling as a potentially novel candidate for transgenic JP2-OE to target atrial dysfunction and heart failure mortality. Thus, adeno-associated (i.e., AAV9) virally mediated gene therapy to restore junctophilin-2 expression, previously shown to slow left ventricular progression of heart failure (43), emerges as an immediate opportunity to treat atrial dysfunction and ultimately limit the aggravating effect on heart failure in future preclinical studies.

Among potential study limitations, transgenic junctophilin-2 expression can affect both atrial and ventricular function. However, baseline ventricular contractility was not affected by transgenic JP2-OE (Supplemental Figure 7). While the αMHC promoter was originally established for ventricular transgene expression, junctophilin-2 immunoblotting showed approximately 5-fold increased atrial junctophilin-2 expression. In contrast, although shRNA-JP2 knockdown was titrated to avoid any mortality from heart failure, we anticipate interdependent and synergistic atrioventricular disease processes (Figure 11A). Accordingly, pressure overload induced atrial and ventricular dysfunction with substantial mortality (Figure 11 and Supplemental Figure 3). Finally, while the super-hub $Ca^{2+}$ signaling model was recently extended across species from mouse to human based on improved cell isolation and live superresolution techniques, isolated human AMs could not be studied alive due to local TAT membrane lesions during cell isolation based on physical tissue dissociation protocols (21).

In summary, we propose a model in which junctophilin-2 clustering at AT-SR junctions is essential for coclustering of highly phosphorylated RyR2 channels and regulated local $Ca^{2+}$ release, as the basis of rapid activation of AMs and atrial contraction to boost ventricular filling. Since the stoichiometric junctophilin-2/RyR2 expression ratio is exceptionally low in human and mouse atria, we propose a model of differential subcellular junctophilin-2 clustering in AMs as a cell-specific mechanism: (a) a higher local junctophilin-2 concentration in junctional SR domains provides high-affinity phospholipid-binding MORN domains (14) that stabilize extensive AT-SR junctions and coclustering of highly phosphorylated RyR2 channels and (b) the majority of less phosphorylated, nonjunctional RyR2 channel clusters showed much less junctophilin-2 locally. In addition, pressure overload resulted in critically decreased junctophilin-2 expression in hypertrophied atria, disrupting JMCs at ATs, resulting in decreased contractility and fibrosis. In contrast, shRNA-mediated knockdown of junctophilin-2 diminished junctional RyR2 clustering without fibrosis but confirmed atrial loss of function. Whereas junctophilin-2 knockdown 3 days

after TAC resulted in 100% mortality, JP2-OE rescued atrial function and prevented any mortality. In conclusion, we show for the first time to our knowledge that JP2-OE in atrial tissue protects from pressure overload–induced heart failure deterioration and premature death in mice. Mechanistically, we identify disruption of junctophilin-2 clustering at AT-SR junctions as causative for the excitation-contraction coupling defect and as a basis for atrial dysfunction. Our results open new avenues for a molecularly informed classification of atrial dysfunction and cardiomyopathy and, ultimately, for the development of therapeutic approaches that prevent atrial dysfunction and heart failure deterioration.

## Methods

Additional information is provided in the Supplemental Methods.

*Mouse cardiomyocyte isolation*. AMs and VMs were isolated from adult mouse hearts using collagenase type II and Langendorff perfusion, as described previously (12, 44). Please see Supplemental Table 2 for the composition of physiological buffer solutions used in our protocols. Generation of MCM-shJP2 and JP2-OE mice was described previously (15). Junctophilin-2 knockdown was adapted for atrial studies, using 1 tamoxifen injection (40 mg/kg i.p.) for 14 or 28 days as indicated. We used adult sex-mixed mouse cohorts of 10–16 weeks age backcrossed into the C57BL/6N background. TAC was induced with a 27G spacer as described previously (45) to induce left ventricular outflow constriction.

*Human cardiac tissues*. For immunofluorescence imaging, atrial and ventricular samples were obtained from patients undergoing open heart surgery, following written informed consent. For clinical patient information please see Supplemental Table 3. Cardiac tissues were fixed in 4% PFA, embedded in paraffin, cut into 4-μm-thick sections, deparaffinized, and rehydrated, and antigens were unmasked in 10 mM sodium citrate buffer prior to antibody incubation.

*Immunofluorescence STED nanoscopy*. Isolated myocytes were fixed with 4% PFA and permeabilized with 0.2% Triton. For detailed information about primary antibodies please refer to Supplemental Table 1. Secondary antibodies were coupled to the fluorophores STAR635P, STAR580, and STAR488 (Abberior Instruments). STED images of isolated myocytes or cardiac tissues were acquired with a Leica TCS SP8 laser-scanning microscope. For imaging settings please refer to the Supplemental Methods. Images were processed in ImageJ/Fiji (NIH), and junctophilin-2/RyR2 cluster segmentation analyses were performed with predefined macros. Junctophilin-2/RyR2 signal overlap was analyzed in corresponding binary images.

*Live-membrane staining*. AMs attached to laminin-coated coverslips were stained with 5 μM Cholesterol-PEG-KK114 (custom-synthesis described in ref. 21) or 40 μM di-8-ANEPPS (Molecular Probes) for 10 minutes. Confocal images were acquired with a Zeiss LSM 880 microscope and a Plan-Apochromat 63×/1.40 oil objective using a pixel size of 100 × 100 nm. Skeletons were extracted from tubular membrane stains for analysis of TAT network components (44). For superresolution imaging of select TAT membrane structures, we used a Leica TCS SP8 STED system with a HC PL APO C2S 100×/1.40 oil objective and a pixel size of 16.23 × 16.23 nm. For imaging settings please refer to the Supplemental Methods. AT diameter was measured as FWHM by Gaussian fitting in line profiles (21). Intracellular $Ca^{2+}$ imaging with fluo-4-AM in Tyrode solution containing 1.2 mM [$Ca^{2+}$] was combined with Cholesterol-PEG-KK114 as described previously (21). For details about the $Ca^{2+}$ spark analysis please refer to the Supplemental Methods.

*ET*. Isolated AMs were high-pressure frozen using a Leica HPM100 system (46). ET for segmentation and 3D reconstruction of AT-SR junctions was performed as described previously (12, 22).

*Sarcomere shortening*. 1-Hz field–stimulated AMs in Tyrode solution containing 1.2 mM [$Ca^{2+}$] were recorded using optical contrast imaging according to the manufacturer's instructions (IonOptix).

*Echocardiography*. Mouse atria were measured in parasternal long-axis view at the level of the aortic valve using simultaneous ECG monitoring (Vevo2100, VisualSonics).

*Western blots*. Cardiac tissue lysates were prepared separately for atrial and ventricular tissue, as described previously (12). For immunoprecipitation, we used a solubilization buffer containing 0.15% CHAPS and incubated 500 μg solubilized protein with 5 μg anti–junctophilin-2 antibody or normal mouse IgG overnight. Dynabeads Protein G (Thermo Fisher Scientific) was added and incubated for 2 hours at 4°C. Please refer to the Supplemental Methods for detailed information. Primary antibodies are listed in Supplemental Table 1. See complete unedited blots in Supplemental Figure 1.

*Statistics*. Statistical analyses were performed in Microsoft Excel 2010, GraphPad Prism 7.03, OriginPro 8.5G, and SigmaPlot 12.3. All data were normally distributed and are presented as mean ± SEM unless

indicated otherwise. Differences were analyzed by 2-tailed unpaired or paired Student's *t* test as appropriate, ANOVA, or log-rank Mantel-Cox testing, as indicated in the figure legends. *P* values of less than 0.05 were accepted to indicate statistical differences.

*Study approval*. All experiments were carried out according to guidelines for the care and use of laboratory animals, following directive 2010/63/EU of the European Parliament and in keeping with NIH guidelines. Animal procedures followed institutional rules as reviewed by the University Medical Center Göttingen IACUC and were approved by the veterinarian state authority (LAVES, Oldenburg, Germany; 33.19-42502-04-15/1924 and 33.9-42502-04-16/2102). Human myocardial samples were used based on informed consent and protocols approved by the ethics committee of the University Medical Center Göttingen (21/10/00).

## Author contributions

BE, EARZ, J. Pawlowitz, SB, and SEL designed the studies. BE, EARZ, GH, J. Pawlowitz, J. Peper, PK, SB, SEL, and TK performed the research and analyzed the data. SS provided expertise about human heart samples and data analysis. GYM performed the custom synthesis of Cholesterol-PEG-KK114. SB, SEL, and XHTW wrote the manuscript, and all authors contributed to the final version.

## Acknowledgments

We are grateful for excellent technical assistance by Birgit Schumann and Brigitte Korff; to Carolin Wichmann for high-pressure freezing sample preparation; and to Martin Schorb from the Electron Microscopy core facility at EMBL Heidelberg. This project was supported by grants from Deutsche Forschungsgemeinschaft to SEL (SFB1002 project A09; service project S02) and to GH (SFB1002 project D01; service project S01) and from DZHK (German Center for Cardiovascular Research), partner site Göttingen, to SEL (DZHK GOE MD3 and MD5). SB received financial support through the clinician scientist program "Translational Medicine" of the University Medical Center Göttingen. The German Cardiac Society supported the doctoral thesis of J. Pawlowitz, and DZHK (German Center for Cardiovascular Research) supported the doctoral theses of BE and J. Pawlowitz. PK acknowledges the European Research Council advanced grant CardioNECT. EARZ is funded by a Emmy Noether Fellowship by Deutsche Forschungsgemeinschaft (no. 396913060). XHTW is supported by NIH grants R01-HL089598, R01-HL091947, and R01-HL117641.

Address correspondence to: Stephan E. Lehnart, University Medical Center Göttingen, Department of Cardiology & Pneumology, Heart Research Center Göttingen, Robert-Koch-Str. 42a, Göttingen 37075, Germany. Phone: 49.551.39.63631; Email: slehnart@med.uni-goettingen.de.

SS's present address is: Department for Internal Medicine II, Cardiology, Pneumology, Intensive Care, University Hospital Regensburg, Regensburg, Germany.

1. Benjamin EJ, et al. Heart disease and stroke statistics—2018 update: A report from the American Heart Association. *Circulation*. 2018;137(12):e67–e492.
2. Wang TJ, et al. Temporal relations of atrial fibrillation and congestive heart failure and their joint influence on mortality: the Framingham Heart Study. *Circulation*. 2003;107(23):2920–2925.
3. Mogensen UM, et al. Type of atrial fibrillation and outcomes in patients with heart failure and reduced ejection fraction. *J Am Coll Cardiol*. 2017;70(20):2490–2500.
4. Kotecha D, et al. Efficacy of β blockers in patients with heart failure plus atrial fibrillation: an individual-patient data meta-analysis. *Lancet*. 2014;384(9961):2235–2243.
5. Heidenreich PA, et al. Forecasting the future of cardiovascular disease in the United States: a policy statement from the American Heart Association. *Circulation*. 2011;123(8):933–944.
6. Yiin GS, et al. Age-specific incidence, outcome, cost, and projected future burden of atrial fibrillation-related embolic vascular events: a population-based study. *Circulation*. 2014;130(15):1236–1244.
7. Goette A, et al. EHRA/HRS/APHRS/SOLAECE expert consensus on atrial cardiomyopathies: Definition, characterization, and clinical implication. *Heart Rhythm*. 2017;14(1):e3–e40.
8. Ahlberg G, et al. Rare truncating variants in the sarcomeric protein titin associate with familial and early-onset atrial fibrillation. *Nat Commun*. 2018;9(1):4316.
9. Peng W, et al. Dysfunction of myosin light-chain 4 (MYL4) leads to heritable atrial cardiomyopathy with electrical, contractile, and structural components: evidence from genetically-engineered rats. *J Am Heart Assoc*. 2017;6(11):e007030.
10. Brandenburg S, Arakel EC, Schwappach B, Lehnart SE. The molecular and functional identities of atrial cardiomyocytes in health and disease. *Biochim Biophys Acta*. 2016;1863(7 Pt B):1882–1893.

11. Guichard JB, Nattel S. Atrial cardiomyopathy: A useful notion in cardiac disease management or a passing fad? *J Am Coll Cardiol*. 2017;70(6):756–765.
12. Brandenburg S, et al. Axial tubule junctions control rapid calcium signaling in atria. *J Clin Invest*. 2016;126(10):3999–4015.
13. Lüss I, et al. Expression of cardiac calcium regulatory proteins in atrium v ventricle in different species. *J Mol Cell Cardiol*. 1999;31(6):1299–1314.
14. Takeshima H, Komazaki S, Nishi M, Iino M, Kangawa K. Junctophilins: a novel family of junctional membrane complex proteins. *Mol Cell*. 2000;6(1):11–22.
15. van Oort RJ, et al. Disrupted junctional membrane complexes and hyperactive ryanodine receptors after acute junctophilin knockdown in mice. *Circulation*. 2011;123(9):979–988.
16. Landstrom AP, et al. Junctophilin-2 expression silencing causes cardiocyte hypertrophy and abnormal intracellular calcium-handling. *Circ Heart Fail*. 2011;4(2):214–223.
17. Wagner E, et al. Stimulated emission depletion live-cell super-resolution imaging shows proliferative remodeling of T-tubule membrane structures after myocardial infarction. *Circ Res*. 2012;111(4):402–414.
18. Beavers DL, et al. Mutation E169K in junctophilin-2 causes atrial fibrillation due to impaired RyR2 stabilization. *J Am Coll Cardiol*. 2013;62(21):2010–2019.
19. Quick AP, et al. Novel junctophilin-2 mutation A405S is associated with basal septal hypertrophy and diastolic dysfunction. *JACC Basic Transl Sci*. 2017;2(1):56–67.
20. Thul R, Coombes S, Roderick HL, Bootman MD. Subcellular calcium dynamics in a whole-cell model of an atrial myocyte. *Proc Natl Acad Sci USA*. 2012;109(6):2150–2155.
21. Brandenburg S, et al. Axial tubule junctions activate atrial $Ca^{2+}$ release across species. *Front Physiol*. 2018;9:1227.
22. Rog-Zielinska EA, Johnston CM, O'Toole ET, Morphew M, Hoenger A, Kohl P. Electron tomography of rabbit cardiomyocyte three-dimensional ultrastructure. *Prog Biophys Mol Biol*. 2016;121(2):77–84.
23. Munro ML, et al. Junctophilin-2 in the nanoscale organisation and functional signalling of ryanodine receptor clusters in cardiomyocytes. *J Cell Sci*. 2016;129(23):4388–4398.
24. Ni L, et al. Atrial-specific gene delivery using an adeno-associated viral vector. *Circ Res*. 2019;124(2):256–262.
25. Guo A, et al. Overexpression of junctophilin-2 does not enhance baseline function but attenuates heart failure development after cardiac stress. *Proc Natl Acad Sci USA*. 2014;111(33):12240–12245.
26. Jiang M, et al. JPH-2 interacts with $Ca_i$-handling proteins and ion channels in dyads: Contribution to premature ventricular contraction-induced cardiomyopathy. *Heart Rhythm*. 2016;13(3):743–752.
27. Nabauer M, et al. The Registry of the German Competence NETwork on Atrial Fibrillation: patient characteristics and initial management. *Europace*. 2009;11(4):423–434.
28. Lindman BR, et al. Calcific aortic stenosis. *Nat Rev Dis Primers*. 2016;2:16006.
29. Chen B, et al. Critical roles of junctophilin-2 in T-tubule and excitation-contraction coupling maturation during postnatal development. *Cardiovasc Res*. 2013;100(1):54–62.
30. Reynolds JO, et al. Junctophilin-2 is necessary for T-tubule maturation during mouse heart development. *Cardiovasc Res*. 2013;100(1):44–53.
31. Guo A, et al. E-C coupling structural protein junctophilin-2 encodes a stress-adaptive transcription regulator. *Science*. 2018;362(6421):null.
32. Voigt N, et al. Cellular and molecular mechanisms of atrial arrhythmogenesis in patients with paroxysmal atrial fibrillation. *Circulation*. 2014;129(2):145–156.
33. Flucher BE, Morton ME, Froehner SC, Daniels MP. Localization of the alpha 1 and alpha 2 subunits of the dihydropyridine receptor and ankyrin in skeletal muscle triads. *Neuron*. 1990;5(3):339–351.
34. Jorgensen AO, Shen AC, Arnold W, Leung AT, Campbell KP. Subcellular distribution of the 1,4-dihydropyridine receptor in rabbit skeletal muscle in situ: an immunofluorescence and immunocolloidal gold-labeling study. *J Cell Biol*. 1989;109(1):135–147.
35. Franzini-Armstrong C, Protasi F, Ramesh V. Shape, size, and distribution of $Ca^{2+}$ release units and couplons in skeletal and cardiac muscles. *Biophys J*. 1999;77(3):1528–1539.
36. Nickel AG, et al. Reversal of mitochondrial transhydrogenase causes oxidative stress in heart failure. *Cell Metab*. 2015;22(3):472–484.
37. Wei S, et al. T-tubule remodeling during transition from hypertrophy to heart failure. *Circ Res*. 2010;107(4):520–531.
38. Xu M, et al. Mir-24 regulates junctophilin-2 expression in cardiomyocytes. *Circ Res*. 2012;111(7):837–841.
39. Wu HD, et al. Ultrastructural remodelling of $Ca^{2+}$ signalling apparatus in failing heart cells. *Cardiovasc Res*. 2012;95(4):430–438.
40. Zhang HB, et al. Ultrastructural uncoupling between T-tubules and sarcoplasmic reticulum in human heart failure. *Cardiovasc Res*. 2013;98(2):269–276.
41. Guo A, et al. Molecular determinants of calpain-dependent cleavage of junctophilin-2 protein in cardiomyocytes. *J Biol Chem*. 2015;290(29):17946–17955.
42. Wang Y, et al. Targeting calpain for heart failure therapy: implications from multiple murine models. *JACC Basic Transl Sci*. 2018;3(4):503–517.
43. Reynolds JO, et al. Junctophilin-2 gene therapy rescues heart failure by normalizing RyR2-mediated Ca. *Int J Cardiol*. 2016;225:371–380.
44. Wagner E, Brandenburg S, Kohl T, Lehnart SE. Analysis of tubular membrane networks in cardiac myocytes from atria and ventricles. *J Vis Exp*. 2014;null(92):e51823.
45. Toischer K, et al. Differential cardiac remodeling in preload versus afterload. *Circulation*. 2010;122(10):993–1003.
46. Vogl C, et al. Unconventional molecular regulation of synaptic vesicle replenishment in cochlear inner hair cells. *J Cell Sci*. 2015;128(4):638–644.